Journal of Non-Newtonian Fluid Mechanics 265 (2019) 99–115

Contents lists available at ScienceDirect

Journal of Non-Newtonian Fluid Mechanics

journal homepage: www.elsevier.com/locate/jnnfm

A coupled finite volume flow solver for the solution of incompressible viscoelastic flows

C. Fernandes[a], V. Vukčević[b,*], T. Uroić[b], R. Simoes[a,c], O.S. Carneiro[a], H. Jasak[b,d], J.M. Nóbrega[a]

[a] Institute for Polymers and Composites/i3N, University of Minho, Campus de Azurém, 4800-058 Guimarães, Portugal
[b] University of Zagreb, Faculty of Mechanical Engineering and Naval Architecture, Ivana Lučića 5, 10000 Zagreb, Croatia
[c] Polytechnic Institute of Cavado and Ave, Campus do IPCA, 4750-810 Barcelos, Portugal
[d] Wikki Ltd, London, United Kingdom

ARTICLE INFO

Keywords:
Coupled solver
Viscoelastic flow
Finite volume method
Openfoam
Computer simulation

ABSTRACT

In this work, a block coupled algorithm for the solution of laminar, incompressible viscoelastic flow problems on collocated grids is presented. The inter-equation coupling of the incompressible Cauchy momentum equations and extra-stress tensor constitutive equation is obtained by deriving a pressure equation in a procedure similar to a SIMPLE algorithm with the Rhie-Chow interpolation technique, and a special treatment of the diffusion term in the momentum equations added by the improved both-sides diffusion (iBSD) technique, recently developed for the finite volume method. Additionally, the velocity field is considered implicitly in the extra-stress tensor constitutive equation by expanding the convective term with a second order Taylor series expansion. All the equations, comprising the continuity, momentum and extra-stress tensor constitutive equations are block-coupled into a single system of equations. The implicitly coupled system of equations is solved by an algebraic multigrid algorithm, which allows to accelerate the calculation process. The performance improvements obtained with the new solver are studied for three 2D viscoelastic flow case studies, and are quantified in terms of number of iterations and CPU time required to reach the predefined convergence criteria. The presented algorithm has been implemented into the open-source computational library foam-extend, a community driven fork of the OpenFOAM software.

1. Introduction

Non-Newtonian fluids proliferate in several aspects of our daily life. They emerge in nature, where most of body fluids, like blood and mucus, are of this type. They are also present in the plastics industry, being used to produce bags, toys, technical profiles, car components, textiles, etc., through extrusion, injection molding, fiber spinning, and other technologies. Molten thermoplastics are viscoelastic fluids, constituting a class of the non-Newtonian group. For this type of fluids a non-linear constitutive equation that includes elastic effects needs to be considered. For an isothermal problem, the set of highly coupled governing equations, consisting of the continuity, the momentum and the constitutive equations, has to be solved [1].

To obtain an approximate solution for the governing equations referred above, a discretization method which approximates the partial differential equations by a system of algebraic equations for the variables at some set of discrete locations in space (elements/cells) and time have to be used. There are many approaches, but the most widely used ones are: the Finite Difference (FD), the Finite Volume (FV) and the Finite Element (FE) methods. The FV approach is perhaps the simplest to implement, and all terms that have to be approximated possess a clear physical meaning, which made it popular among engineers. On the basis of the FV discretization is the variable arrangement, defining the storage location of the flow variables. Usually, the cell-centered variable arrangement is preferred within the FV method, but vertex-centered variable arrangement has also been used [2]. In a vertex-centered arrangement the flow variables are stored at the vertices (or grid points), with control volumes constructed around the variable locations, by using the concept of a dual mesh and dual cells [2]. The major disadvantage of this approach is the need to base the mesh on a set of element types for which a shape function can be defined. In the cell-centered variable arrangement the variables and their related quantities are stored at the centroids of the grid cells, which is more advantageous as it leads to a more straightforward computer code implementation.

After the discretization process has been chosen, another issue to be addressed to solve the Navier-Stokes equations is the coupling between pressure and velocity fields. Generally, this can be done following either a segregated or a coupled approach. In the segregated approach, the systems of equations for all variables are solved sequentially using fixed, best-estimate values of other dependent variables [3–14]. This is in contrast with the coupled approach, in which the discretized equations of

* Corresponding author.
E-mail address: vuko.vukcevic@fsb.hr (V. Vukčević).

https://doi.org/10.1016/j.jnnfm.2019.01.006
Received 1 November 2017; Received in revised form 8 January 2019; Accepted 20 January 2019
Available online 7 February 2019

all variables are solved simultaneously in a single system of equations [15–23], where the explicit contributions are minimized.

In the segregated approach the use of pressure-correction/fractional step schemes, to overcome the difficulty to couple pressure with velocity in time-dependent viscous incompressible flows, started in the late 1960s with the ground breaking work of Chorin [3] and Temam [4], who developed the non-incremental pressure-correction scheme. However, the segregated approach acquired popularity in the early 1970s by the Computational Fluid Dynamics (CFD) group at Imperial College through the development of the SIMPLE algorithm (Semi-Implicit Method for Pressure Linked Equations) [5] for the solution of incompressible flows. The major advantages of the SIMPLE algorithm were the low memory requirement and coding simplicity, which were key factors given the state of computer technology at that time [20]. Further developments were subsequently undertaken, which led to a family of SIMPLE-like algorithms [6,9], a review of which is reported in [14]. Additionally, Issa [10] developed a non-iterative method for handling the pressure-velocity coupling of the implicitly discretized fluid flow equations. The method called PISO, for Pressure-Implicit with Splitting of Operators, utilizes the splitting of operations in the solution of the discretized momentum and pressure equations so that the fields obtained at each time-step are close approximations of the exact solution. Later, van Kan [11] developed a second-order (in space) incremental pressure-correction scheme, by considering the pressure gradient term explicitly in the momentum equations and then correcting the velocity in the continuity equation. More accurate (second-order in time) fractional step schemes were proposed (see Dean and Glowinski [13] for a framework and Brown et al. [24] for a review).

The previous formulations were prone to checkerboard patterns, which were visible between the pressure and velocity fields. This problem can be fixed either by using both a staggered or a collocated grid arrangement. In the staggered grid the velocity field is stored at cell faces, while pressure and all other variables are stored at cell centroids. On this arrangement, the pressure gradient is related with consecutive grid points values, straddling the element face, without interpolation need. Nevertheless, adopting a staggered grid arrangement has its disadvantages, besides the memory requirement to store a grid system for every velocity component and another for pressure and other variables, the staggering procedure itself becomes an issue for non-Cartesian grids, and even more complex if unstructured grids are considered. Therefore, it turns out that the use of a cell-centered collocated grid system, where all variables are stored at the cell centroid, is a more attractive solution, with the mass flux, a scalar value, being stored at the element faces. To assure the coupling between the velocity and pressure fields, mass flux is computed using a custom interpolation of the discrete momentum equation, known as the Rhie-Chow [8] interpolation. The work of these researchers and that of Hsu [7] provided a solution to the checkerboard problem and expanded the application area of the SIMPLE-like algorithms by enabling the use of a collocated variable arrangement [12].

Subsequently, the extension of the SIMPLE-like segregated algorithms to a wide range of fluid physics was done, namely for non-Newtonian viscoelastic [25–31] fluid flows. When solving numerically the flow of viscoelastic fluids, the High Weissenberg Number Problem (HWNP) has been addressed over the last decades as one of the main difficulties to be handled. This is related to the loss of convergence of the iterative procedure for solving the non-linear system of governing differential equations, which is attributed to several causes (see [32–37]). Although a wide spectrum of techniques and problems have been investigated, most of the published work deals with mixed finite element methods [38–42] or in the FVM framework follow a segregated approach (e.g. log-conformation [43]). However, the codes implemented with a segregated approach are prone to divergence [44] because each field is updated sequentially with different equations. Thus, require the use of large relaxation factors (e.g. 0.3 for pressure and stress fields) increasing the computational time, specially for viscoelastic flows.

Aiming to reduce the calculation time and tendency for divergence, several coupled algorithms for inelastic fluids have been reported in the literature, which can be divided into two groups [20,21]. In the first group, the Navier-Stokes equations are discretized in a direct way, i.e., the continuity equation is enforced meaning that no pressure equation is derived [45–49]. Examples of these algorithms include the SIVA (simultaneous variable arrangement) algorithm of Caretto et al. [45], the method of Braaten [46], the SCGS (symmetric coupled Gauss Seidel) algorithm of Vanka [47], the UVP method of Karki and Mongia [48], and more recently the BIP (Body Implicit Procedure) of Mazhar [49]. The absence of a pressure equation in these algorithms leads to an ill-conditioned system of equations, because of zero values present in the main diagonal of the continuity equation [20]. In the second group, a pressure equation is derived, yielding an extended set of diagonally dominant equations [20]. Generally, two approaches are followed within this second group. In the first [19], a pressure equation involving pseudo-velocities, as in the SIMPLER algorithm [6], is used. In the second, a segregated pressure equation is devised without adding new variables [15], as in the SIMPLE algorithm [5]. Using the control volume finite element method (CVFEM), Lonsdale [16] followed the second approach and reported large convergence rates and good scaling behavior with dense meshes. However, the algorithm did not prove to be robust [17]. In a subsequent work, using the Rhie-Chow interpolation, Webster [17,18] improved Lonsdale's algorithm [16] and showed a substantial increase of convergence rate and decrease in computational time. In the context of the FVM formulation, Darwish et al. [20] implemented a pressure-based coupled algorithm for the solution of incompressible flow problems over structured grid systems in the open-source computational library OpenFOAM, which can be viewed as a continuation of the work of Webster [18]. Their results showed that, for the problems presented, the CPU time per control volume is nearly independent of the grid size. Subsequently, the work was extended to unstructured grids [21], and the results showed a substantial decrease in CPU time using the coupled approach when compared to the segregated method, with the gains increasing with the grid size. Later, Chen and Przekwas [22] developed a pressure-based coupled solution approach for incompressible or subsonic compressible flows. The velocity, pressure and temperature are obtained at the same time by solving simultaneously the Navier-Stokes momentum, the mass continuity and the energy equations. Again, excellent results were achieved in terms of numerical convergence and reduction of CPU time. Finally, Mangani et al. [23] developed a block coupled algorithm for the solution of incompressible turbulent flows. The simultaneous solution of momentum and continuity equations is obtained by implicit block coupling of pressure and velocity, and a two-equation eddy viscosity turbulence model is solved in a segregated fashion. The scalability of the coupled solution algorithm with increasing number of cells was found to be almost linear. These works showed that when dealing with inelastic fluids the computational time can be reduced using a fully coupled solver. Therefore, it is worth to expand the method to viscoelastic flows for which the segregated algorithm, employed until now, presents several stability issues [50], that requires the use of large relaxation factors and limits the maximum achievable Deborah/Weissenberg numbers if the log-conformation approach is not used [43].

In this paper a new numerical code is developed in the context of the FVM following a coupling approach to compute the flow of viscoelastic fluids. For the best of the authors knowledge, this is the first attempt to expand the concept of coupled solvers to viscoelastic flows. The code is implemented in the open-source computational library foam-extend [51], a community driven fork of the OpenFOAM software. The solution of the enlarged system of equations, composed by continuity, momentum and extra-stress constitutive equations, is obtained using an algebraic multigrid solver. The performance of the coupled viscoelastic solver is assessed with three case studies, namely the Oldroyd-B Poiseuille, the UCM lid-driven cavity and the LPTT 4:1 sudden contraction planar flows. The main target is to assess the performance, in terms

of the number of iterations and CPU time, of the coupled algorithm with increasing mesh density and Deborah number, when compared with the previously developed segregated solver [50] based on the SIMPLE algorithm. Additionally, for assessment purposes, the results obtained with the developed code are compared with analytical solutions, results obtained with the segregated viscoelastic solver [50], and with some additional solutions presented in the scientific literature.

The remainder sections of the paper are organized as follows. First, the governing equations of the viscoelastic flow studied in this work are presented. Then, the numerical procedure of the coupled algorithm will be described in detail, including the finite-volume discretization process and the steps followed by the proposed coupled algorithm. Finally, the performance of the numerical code will be assessed using the three case studies mentioned on the last paragraph, aiming to highlight the advantages of the coupled approach. The paper ends with the main conclusions.

2. Governing equations

The basic equations governing transient, incompressible and isothermal laminar flows of viscoelastic fluids are the continuity, momentum and constitutive equations. The continuity and momentum equations read:

$$\nabla \cdot (\rho \mathbf{u}) = 0 \tag{1}$$

$$\frac{\partial(\rho \mathbf{u})}{\partial t} + \nabla \cdot (\rho \mathbf{u}\mathbf{u}) + \nabla \cdot (p\mathbf{I}) - \nabla \cdot \boldsymbol{\tau} = 0 \tag{2}$$

where ρ is the fluid density, $\mathbf{u}$ is the velocity vector, t is the time, p is the pressure, $\mathbf{I}$ is the identity tensor and $\boldsymbol{\tau}$ is the total extra-stress tensor, which is split into solvent ($\boldsymbol{\tau}_S$) and polymeric ($\boldsymbol{\tau}_P$) contributions, such that $\boldsymbol{\tau} = \boldsymbol{\tau}_S + \boldsymbol{\tau}_P$. Both stress terms are obtained by the following equations, which form the constitutive model

$$\boldsymbol{\tau}_S = \eta_S \left(\nabla \mathbf{u} + \nabla \mathbf{u}^T\right) \tag{3}$$

$$f(\mathrm{tr}(\boldsymbol{\tau}_P))\boldsymbol{\tau}_P + \lambda\left(\frac{\partial \boldsymbol{\tau}_P}{\partial t} + \nabla \cdot (\mathbf{u}\boldsymbol{\tau}_P)\right) = \eta_P\left(\nabla \mathbf{u} + \nabla \mathbf{u}^T\right) + \lambda\left(\boldsymbol{\tau}_P \cdot \nabla \mathbf{u} + \nabla \mathbf{u}^T \cdot \boldsymbol{\tau}_P\right) \tag{4}$$

where η_S and η_P are the solvent and polymeric viscosities, respectively, λ is the polymer relaxation time, and the stress function $f(\mathrm{tr}(\boldsymbol{\tau}_P))$ follows the linear form of the PTT model [52]:

$$f(\mathrm{tr}(\boldsymbol{\tau}_P)) = 1 + \frac{\lambda \epsilon}{\eta_P}\mathrm{tr}(\boldsymbol{\tau}_P) \tag{5}$$

where ϵ is the extensibility parameter.

The constitutive equation for the polymeric component of the extra-stress tensor ($\boldsymbol{\tau}_P$) is given by Eq. (4). As previously referred, we apply the LPTT model [52] ($\epsilon \neq 0$), the Oldroyd-B model [53] ($\epsilon = 0$ and $\eta_S \neq 0$) and the UCM model ($\epsilon = 0$ and $\eta_S = 0$) as the viscoelastic fluid models. For these models, a characteristic (solvent) viscosity ratio can be defined by $\beta = \eta_S/(\eta_S + \eta_P) = \eta_S/\eta_0$, known as retardation ratio, where η_0 is the total viscosity in the limit of vanishing shear rate.

The divergence of $\boldsymbol{\tau}_S$ will appear in the momentum equation (Eq. (2)) as a diffusive term ($\nabla \cdot (\eta_S \nabla \mathbf{u})$) to be discretized implicitly (note that $\nabla \cdot (\eta_S \nabla \mathbf{u}^T) = 0$). In the framework of the coupled viscoelastic solver developed in this work, the divergence of $\boldsymbol{\tau}_P$ is discretized implicitly (differently from the usual segregated approach where this term is discretized explicitly). Additionally, a standard approach to avoid numerical instabilities, which arise when simulating viscoelastic fluids, is to add a stabilizing diffusive term ($\nabla \cdot (\eta^\star \nabla \mathbf{u})$) to both sides of Eq. (2), one being discretized implicitly (LHS) and the other explicitly (RHS), a technique known as both-sides diffusion (BSD) [54],

$$\frac{\partial(\rho \mathbf{u})}{\partial t} + \nabla \cdot (\rho \mathbf{u}\mathbf{u}) - \nabla \cdot \left[(\eta_S + \eta^\star)\nabla \mathbf{u}\right] + \nabla \cdot (p\mathbf{I}) - \nabla \cdot \boldsymbol{\tau}_P = -\nabla \cdot (\eta^\star \nabla \mathbf{u}) \tag{6}$$

where $\eta^\star$ is a viscosity coefficient proportional to the polymer viscosity η_P, here defined as $\eta^\star = \eta_P$. The new stress-velocity coupling formulation developed by Fernandes et al. [50] is used to couple the velocity and stress fields. In practice, the stress-velocity coupling is achieved by replacing the explicit diffusive term of the BSD technique with a special second-order derivative of the velocity field, as described in Section 3.1, a methodology known as iBSD [50], improved both-sides diffusion.

3. Numerical method

In this section, we will describe the mathematical formulation used to setup a coupled solver procedure to solve the continuity, momentum and constitutive equations simultaneously. This will be split into several sub-sections, one for each set of equations to be solved.

In the segregated SIMPLE algorithm [5], the solution is obtained by iteratively solving the momentum equations and a pressure correction equation, which was derived from the continuity equation, while accounting for the effects of the pressure field on the momentum equations through a correction of the velocity field. The convergence of the SIMPLE algorithm is highly affected by the explicit treatment of the pressure gradient in the momentum equations and the velocity field in the continuity equation. In the framework of the coupled solver developed in this work both terms are treated in an implicit manner. In addition, to take into account the influence of the velocity field in the stress constitutive equation, the advective term in Eq. (4) is discretized implicitly using a Taylor series expansion, as described in Section 3.3. The devised methodology is only explained and illustrated for structured grids, but the implementation is general and can be used on unstructured grids. Moreover, to facilitate the understanding of the methodology this will be described assuming a structured 2D grid, but the developed code was implemented in an unstructured 3D grid.

3.1. Discretization of the momentum equations

Following the FVM procedure, the discretization starts by integrating the momentum equations (Eq. (6)) over a general control volume V, illustrated in Fig. 1, to yield

$$\int_V \frac{\partial(\rho \mathbf{u})}{\partial t}\,\mathrm{d}V + \int_V \nabla \cdot (\rho \mathbf{u}\mathbf{u})\,\mathrm{d}V - \int_V \nabla \cdot \left[(\eta_S + \eta^\star)\nabla \mathbf{u}\right]\mathrm{d}V + \int_V \nabla \cdot (p\mathbf{I})\,\mathrm{d}V - \int_V \nabla \cdot \boldsymbol{\tau}_P\,\mathrm{d}V = -\int_V \nabla \cdot (\eta^\star \nabla \mathbf{u})\,\mathrm{d}V \tag{7}$$

Using the Gauss divergence theorem, the volume integrals of the advection, diffusion, pressure and polymeric extra-stress tensor terms in Eq. (7) are transformed into surface integrals as

$$\int_V \frac{\partial(\rho \mathbf{u})}{\partial t}\,\mathrm{d}V + \oint_S \mathbf{n} \cdot (\rho \mathbf{u}\mathbf{u})\,\mathrm{d}S - \oint_S \mathbf{n} \cdot \left[(\eta_S + \eta^\star)\nabla \mathbf{u}\right]\mathrm{d}S + \oint_S \mathbf{n} \cdot (p\mathbf{I})\,\mathrm{d}S - \oint_S \mathbf{n} \cdot \boldsymbol{\tau}_P\,\mathrm{d}S = -\oint_S \mathbf{n} \cdot (\eta^\star \nabla \mathbf{u})\,\mathrm{d}S \tag{8}$$

where S is the boundary of control volume V and $\mathbf{n}$ the outward pointing unit vector normal to S.

Then, evaluating the surface integrals using a second order integration scheme and a backward implicit Euler scheme to discretize the rate of change term, the following semi-discretized equation is obtained

$$V_P \rho_P \frac{\mathbf{u}_P - \mathbf{u}_P^0}{\Delta t} + \sum_{f=nb(P)} \mathbf{S}_f \cdot (\rho \mathbf{u}\mathbf{u})_f - \sum_{f=nb(P)} \mathbf{S}_f \cdot \left[(\eta_S + \eta^\star)\nabla \mathbf{u}\right]_f + \sum_{f=nb(P)} \mathbf{S}_f p_f - \sum_{f=nb(P)} \mathbf{S}_f \cdot (\boldsymbol{\tau}_P)_f = -\sum_{f=nb(P)} \mathbf{S}_f \cdot (\eta^\star \nabla \mathbf{u})_f \tag{9}$$

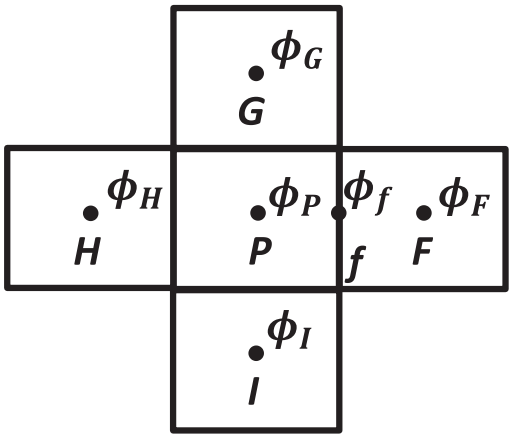

Fig. 1. Schematic representation of the control volume V with centroid P (owner) and with neighboring control volumes with centroids F, G, H and I. The face shared by the control volumes with centroids P and F is represented by f. ϕ holds the value of the variable in the location indicated by the subscript.

where Δt is the time-step, the subscript P refers to values of the variables at control-volume with centroid P and volume V_P, the superscript 0 represents the previous time step value, *nb* refers to values at the faces f, obtained by interpolation between P and its neighbors, and $\mathbf{S}_f$ is the area normal vector to face f.

Finally, the equations are transformed into the algebraic form by expressing the variation in the dependent variable and its derivatives in terms of the control volume P and its neighbors values, at the respective centroids. The discretized algebraic governing equations are given by

$$\begin{cases} a_P^{uu}u_P + a_P^{uv}v_P + a_P^{up}p_P + a_P^{u\tau_{xx}}(\tau_{xx})_P + a_P^{u\tau_{xy}}(\tau_{xy})_P \\ \quad + \sum_{F=NB(P)} a_F^{uu}u_F + \sum_{F=NB(P)} a_F^{uv}v_F \\ + \sum_{F=NB(P)} a_F^{up}p_F + \sum_{F=NB(P)} a_F^{u\tau_{xx}}(\tau_{xx})_F + \sum_{F=NB(P)} a_F^{u\tau_{xy}}(\tau_{xy})_F = b_P^u \\ a_P^{vu}u_P + a_P^{vv}v_P + a_P^{vp}p_P + a_P^{v\tau_{xy}}(\tau_{xy})_P + a_P^{v\tau_{yy}}(\tau_{yy})_P \\ \quad + \sum_{F=NB(P)} a_F^{vu}u_F + \sum_{F=NB(P)} a_F^{vv}v_F \\ + \sum_{F=NB(P)} a_F^{vp}p_F + \sum_{F=NB(P)} a_F^{v\tau_{xy}}(\tau_{xy})_F + \sum_{F=NB(P)} a_F^{v\tau_{yy}}(\tau_{yy})_F = b_P^v \end{cases} \tag{10}$$

where $a_P^{\epsilon\phi}$ and $a_F^{\epsilon\phi}$ are the owner and neighbor coefficients in the discretized momentum equations representing the velocity component ϵ and the variable ϕ interactions, respectively; b_P^{ϵ} is the source term, with the superscript ϵ representing the ϵ velocity component equation (for 2D cases, (u, v)), and $NB(P)$ refers to the neighbors of the control-volume with centroid P.

The first term in Eq. (9), the rate of change (*rchg*), contributes both for the diagonal of the system of equations and for the explicit term as:

$$\begin{aligned} a_{P,rchg}^{uu} &= a_{P,rchg}^{vv} = \frac{V_P\ \rho_P}{\Delta t} \\ b_{P,rchg}^{u} &= \frac{V_P\ \rho_P\ u_P^0}{\Delta t}, \qquad b_{P,rchg}^{v} = \frac{V_P\ \rho_P\ v_P^0}{\Delta t} \end{aligned} \tag{11}$$

The advection term in Eq. (9) is linearized by computing the mass flow rate at control-volume face f ($\dot{m}_f = \mathbf{S}_f \cdot (\rho\mathbf{u})_f$) using the previous iteration values. In this work two different discretization schemes are used to approximate the advection term: the first-order Upwind (UDS) and the high-order CUBISTA (third or second order in uniform or non-uniform grids, respectively) [55] differencing schemes. However, many high-resolution schemes could be used. For the sake of readability the discretization procedure will be presented for the UDS scheme, but it is important to stress that the methodology is independent of the discretization scheme adopted. Hence, considering a first-order upwind discretization, the coefficients of the advection (*adv*) term contribution for the momentum equations are given by

$$\begin{aligned} a_{F,adv}^{uu} &= a_{F,adv}^{vv} = \max(\dot{m}_f,\ 0) \\ a_{P,adv}^{uu} &= -\sum_{F=NB(P)} a_{F,adv}^{uu}, \qquad a_{P,adv}^{vv} = -\sum_{F=NB(P)} a_{F,adv}^{vv} \\ a_{F,adv}^{uv} &= a_{F,adv}^{vu} = 0 \\ a_{P,adv}^{uv} &= -\sum_{F=NB(P)} a_{F,adv}^{uv}, \qquad a_{P,adv}^{vu} = -\sum_{F=NB(P)} a_{F,adv}^{vu} \end{aligned} \tag{12}$$

where, for example, the superscript $\epsilon\phi$ means the influence of the ϕ velocity component in the ϵ velocity component momentum equation. The term $\max(\dot{m}_f,\ 0)$ represents the maximum of $\dot{m}_f$ and 0, where the mass flux is positive if it goes from owner to neighbor cells, i.e. leaves the control-volume V. Some coefficients are null in Eq. (12), but their inclusion is necessary for the proper implementation of the algebraic solver [20,21].

The implicit diffusion (*idiff*) contribution, third term of Eq. (9), is discretized taking a linear profile (see page 86 of [56]) as

$$\mathbf{S}_f \cdot \left[(\eta_S + \eta^\star)\nabla\mathbf{u}\right]_f = (\eta_S + \eta^\star)\frac{\mathbf{S}_f \cdot \mathbf{S}_f}{\mathbf{d}_{PF} \cdot \mathbf{S}_f}(\mathbf{u}_F - \mathbf{u}_P) \tag{13}$$

where $\mathbf{d}_{PF}$ is the vector joining the centroids P and F (see Fig. 1). The coefficients of that term for the momentum equations are given by

$$\begin{aligned} a_{F,idiff}^{uu} &= a_{F,idiff}^{vv} = -(\eta_S + \eta^\star)\frac{\mathbf{S}_f \cdot \mathbf{S}_f}{\mathbf{d}_{PF} \cdot \mathbf{S}_f} \\ a_{P,idiff}^{uu} &= -\sum_{F=NB(P)} a_{F,idiff}^{uu}, \qquad a_{P,idiff}^{vv} = -\sum_{F=NB(P)} a_{F,idiff}^{vv} \\ a_{F,idiff}^{uv} &= a_{F,idiff}^{vu} = 0 \\ a_{P,idiff}^{uv} &= -\sum_{F=NB(P)} a_{F,idiff}^{uv}, \qquad a_{P,idiff}^{vu} = -\sum_{F=NB(P)} a_{F,idiff}^{vu} \end{aligned} \tag{14}$$

The pressure gradient term is discretized assuming a linear variation between the cell centers, thus the cell face pressure can be obtained by linear interpolation

$$p_f = g_f p_P + (1 - g_f)p_F \tag{15}$$

where g_f represents the linear interpolation weight. Hence, the coefficients of the pressure gradient term contribution for the momentum equations are given by

$$\begin{aligned} a_F^{up} &= S_f^x(1 - g_f), \qquad a_F^{vp} = S_f^y(1 - g_f) \\ a_P^{up} &= \sum_{f=nb(P)} S_f^x g_f, \qquad a_P^{vp} = \sum_{f=nb(P)} S_f^y g_f \end{aligned} \tag{16}$$

where S_f^x and S_f^y are, respectively, the x and y components of the surface area vector $\mathbf{S}_f$.

For the divergence of the extra-stress tensor term, the same approach as the one applied for the pressure gradient term was used, and the face extra-stress tensor is obtained by linear interpolation of the values of the two adjacent control volumes

$$(\boldsymbol{\tau}_P)_f = g_f(\boldsymbol{\tau}_P)_P + (1 - g_f)(\boldsymbol{\tau}_P)_F \tag{17}$$

Hence, the coefficients of the extra-stress tensor divergence term contribution for the momentum equations are given by

$$
\begin{aligned}
a_F^{u\tau_{xx}} &= -S_f^x(1-g_f), \qquad a_F^{u\tau_{xy}} = -S_f^y(1-g_f)\\
a_P^{u\tau_{xx}} &= -\sum_{f=nb(P)} S_f^x g_f, \qquad a_P^{u\tau_{xy}} = -\sum_{f=nb(P)} S_f^y g_f\\
a_F^{v\tau_{xy}} &= -S_f^x(1-g_f), \qquad a_F^{v\tau_{yy}} = -S_f^y(1-g_f)\\
a_P^{v\tau_{xy}} &= -\sum_{f=nb(P)} S_f^x g_f, \qquad a_P^{v\tau_{yy}} = -\sum_{f=nb(P)} S_f^y g_f
\end{aligned} \tag{18}
$$

Finally, the explicit diffusion term present in Eq. (9) is given by a special second-order derivative, which contributes to the coupling between the velocity and the extra-stress tensor fields, as described in detail in Fernandes et al. [50]. The discretization of this term is given by

$$
\begin{aligned}
&\mathbf{S}_f \cdot (\eta^\star \nabla \mathbf{u})_f\\
&\quad = \mathbf{S}_f \cdot \eta^\star \left[g_f (\nabla \mathbf{u})_P^0 + (1-g_f)(\nabla \mathbf{u})_F^0 \right]\\
&\quad = \mathbf{S}_f \cdot \eta^\star \left[g_f \left(\frac{1}{V_P} \sum_{f=nb(P)} \mathbf{S}_f \mathbf{u}_f^0 \right) + (1-g_f) \left(\frac{1}{V_F} \sum_{f=nb(F)} \mathbf{S}_f \mathbf{u}_f^0 \right) \right]
\end{aligned} \tag{19}
$$

where the face gradient of $\mathbf{u}^0$, $(\nabla \mathbf{u})_f^0$, is calculated as a linear interpolation of the cell-centred gradient of $\mathbf{u}^0$ for the two cells sharing the face [56]. The coefficients of the explicit diffusion (*ediff*) term contribution for the momentum equations are then given by

$$
\begin{aligned}
b_{P,ediff}^u &= -\eta^\star \left[g_f \left(\frac{1}{V_P} \sum_{f=nb(P)} \left((S_f^x)^2 + (S_f^y)^2 \right) u_f^0 \right) \right.\\
&\qquad \left. + (1-g_f) \left(\frac{1}{V_F} \sum_{f=nb(F)} \left((S_f^x)^2 + (S_f^y)^2 \right) u_f^0 \right) \right]\\
b_{P,ediff}^v &= -\eta^\star \left[g_f \left(\frac{1}{V_P} \sum_{f=nb(P)} \left((S_f^x)^2 + (S_f^y)^2 \right) v_f^0 \right) \right.\\
&\qquad \left. + (1-g_f) \left(\frac{1}{V_F} \sum_{f=nb(F)} \left((S_f^x)^2 + (S_f^y)^2 \right) v_f^0 \right) \right]
\end{aligned} \tag{20}
$$

Notice that the owner and neighbor coefficients related to velocity components interactions are given by the sum of the rate of change, advection and implicit diffusion term contributions

$$
a_\alpha^{\epsilon\phi} = a_{\alpha,rchg}^{\epsilon\phi} + a_{\alpha,adv}^{\epsilon\phi} + a_{\alpha,idiff}^{\epsilon\phi} \tag{21}
$$

where ϵ and ϕ can be either u or v and α can be either P or F. Additionally, the explicit terms of the momentum equations are given by the sum of the rate of change and explicit diffusion terms

$$
b_P^\epsilon = b_{P,rchg}^\epsilon + b_{P,ediff}^\epsilon \tag{22}
$$

where again ϵ can be either u or v.

For the discretization of the continuity equation presented in Section 3.2 the Rhie-Chow [8] interpolation technique is used. For that derivation it is suitable to write the discretized momentum equations, Eq. (10), for each cell as

$$
\begin{cases}
a_P^{uu} u_P + a_P^{uv} v_P + a_P^{u\tau_{xx}} (\tau_{xx})_P + a_P^{u\tau_{xy}} (\tau_{xy})_P + \sum_{F=NB(P)} a_F^{uu} u_F + \sum_{F=NB(P)} a_F^{uv} v_F\\
\quad + \sum_{F=NB(P)} a_F^{u\tau_{xx}} (\tau_{xx})_F + \sum_{F=NB(P)} a_F^{u\tau_{xy}} (\tau_{xy})_F + V_P \frac{\partial p_P}{\partial x} = b_P^u\\
a_P^{vu} u_P + a_P^{vv} v_P + a_P^{v\tau_{xy}} (\tau_{xy})_P + a_P^{v\tau_{yy}} (\tau_{yy})_P + \sum_{F=NB(P)} a_F^{vu} u_F + \sum_{F=NB(P)} a_F^{vv} v_F\\
\quad + \sum_{F=NB(P)} a_F^{v\tau_{xy}} (\tau_{xy})_F + \sum_{F=NB(P)} a_F^{v\tau_{yy}} (\tau_{yy})_F + V_P \frac{\partial p_P}{\partial y} = b_P^v
\end{cases} \tag{23}
$$

where the pressure gradient term, assumed to be constant on each cell, is explicitly shown. Since the cross-coupling velocity coefficients are null (see Eqs. (12) and (14)), Eq. (23) can equivalently be written as

$$
\begin{cases}
u_P + \dfrac{a_P^{u\tau_{xx}} (\tau_{xx})_P + a_P^{u\tau_{xy}} (\tau_{xy})_P + \sum_{F=NB(P)} a_F^{uu} u_F + \sum_{F=NB(P)} a_F^{u\tau_{xx}} (\tau_{xx})_F + \sum_{F=NB(P)} a_F^{u\tau_{xy}} (\tau_{xy})_F - b_P^u}{a_P^{uu}}\\
\quad + \dfrac{V_P}{a_P^{uu}} \dfrac{\partial p_P}{\partial x} = 0\\
v_P + \dfrac{a_P^{v\tau_{xy}} (\tau_{xy})_P + a_P^{v\tau_{yy}} (\tau_{yy})_P + \sum_{F=NB(P)} a_F^{vv} v_F + \sum_{F=NB(P)} a_F^{v\tau_{xy}} (\tau_{xy})_F + \sum_{F=NB(P)} a_F^{v\tau_{yy}} (\tau_{yy})_F - b_P^v}{a_P^{vv}}\\
\quad + \dfrac{V_P}{a_P^{vv}} \dfrac{\partial p_P}{\partial y} = 0
\end{cases} \tag{24}
$$

This leads to the momentum equations written in operator form as

$$
\mathbf{u}_P + \mathbf{H}_P[\mathbf{u}] = -\nabla p_P \cdot \mathbf{D}_P \tag{25}
$$

with each component of $\mathbf{H}_P[\mathbf{u}]$ given by

$$
\begin{aligned}
\mathbf{H}_P[u] &= \frac{a_P^{u\tau_{xx}} (\tau_{xx})_P + a_P^{u\tau_{xy}} (\tau_{xy})_P + \sum_{F=NB(P)} a_F^{uu} u_F + \sum_{F=NB(P)} a_F^{u\tau_{xx}} (\tau_{xx})_F + \sum_{F=NB(P)} a_F^{u\tau_{xy}} (\tau_{xy})_F - b_P^u}{a_P^{uu}}\\
\mathbf{H}_P[v] &= \frac{a_P^{v\tau_{xy}} (\tau_{xy})_P + a_P^{v\tau_{yy}} (\tau_{yy})_P + \sum_{F=NB(P)} a_F^{vv} v_F + \sum_{F=NB(P)} a_F^{v\tau_{xy}} (\tau_{xy})_F + \sum_{F=NB(P)} a_F^{v\tau_{yy}} (\tau_{yy})_F - b_P^v}{a_P^{vv}}
\end{aligned} \tag{26}
$$

and $\mathbf{D}_P$ defined as

$$
\mathbf{D}_P = \begin{pmatrix} \frac{V_P}{a_P^{uu}} & 0 \\ 0 & \frac{V_P}{a_P^{vv}} \end{pmatrix} \tag{27}
$$

3.2. Discretization of the continuity equation

The discretization of the continuity equation, Eq. (1), starts with the integration over the control volume V to yield

$$
\int_V \nabla \cdot (\rho \mathbf{u}) \, \mathrm{d}V = 0 \tag{28}
$$

Again, using the divergence theorem, the volume integral is transformed into a surface integral as

$$\oint_S \mathbf{n}\cdot(\rho\mathbf{u})\,\mathrm{d}S = 0 \tag{29}$$

Hence, the semi-discretized form of the continuity equation is given by

$$\sum_{f=nb(P)} \mathbf{S}_f\cdot(\rho\mathbf{u})_f = 0 \tag{30}$$

In a collocated framework, the velocity at the face is obtained by reconstructing a pseudo-momentum equation at the face from the momentum equations of the straddling cells P and F, known as the Rhie-Chow interpolation [8]. Using Eq. (25), the momentum equations of cells P and F are given by

$$\mathbf{u}_P + \mathbf{H}_P[\mathbf{u}] = -\nabla p_P\cdot\mathbf{D}_P \qquad \text{and} \qquad \mathbf{u}_F + \mathbf{H}_F[\mathbf{u}] = -\nabla p_F\cdot\mathbf{D}_F \tag{31}$$

Hence, the velocity at face f, $\mathbf{u}_f$, straddling the control volumes P and F can be computed by a pseudo-momentum equation as

$$\mathbf{u}_f + \mathbf{H}_f[\mathbf{u}] = -\nabla p_f\cdot\mathbf{D}_f \tag{32}$$

In the spirit of a collocated FVM approach, where the variables are stored at the cell centers, a simple linear interpolation profile is used to compute the coefficients of Eq. (32),

$$\begin{aligned}\mathbf{H}_f[\mathbf{u}] &= g_f\mathbf{H}_P[\mathbf{u}] + (1-g_f)\mathbf{H}_F[\mathbf{u}] = \overline{\mathbf{H}_f}[\mathbf{u}]\\ \mathbf{D}_f &= g_f\mathbf{D}_P + (1-g_f)\mathbf{D}_F = \overline{\mathbf{D}_f}\end{aligned} \tag{33}$$

Substituting Eq. (33) in Eq. (32) we obtain

$$\mathbf{u}_f + \overline{\mathbf{H}_f}[\mathbf{u}] = -\nabla p_f\cdot\overline{\mathbf{D}_f} \tag{34}$$

The next step is to write the coefficient $\overline{\mathbf{H}_f}[\mathbf{u}]$ in terms of velocity and pressure. Combining Eqs. (31) and (33) we obtain

$$\begin{aligned}\overline{\mathbf{H}_f}[\mathbf{u}] &= g_f\left[-\mathbf{u}_P - \nabla p_P\cdot\mathbf{D}_P\right] + (1-g_f)\left[-\mathbf{u}_F - \nabla p_F\cdot\mathbf{D}_F\right]\\ &= -\overline{\mathbf{u}_f} - \overline{\nabla p_f}\cdot\overline{\mathbf{D}_f}\end{aligned} \tag{35}$$

where $\overline{\mathbf{u}_f} = g_f\mathbf{u}_P + (1-g_f)\mathbf{u}_F$. Hence, the face velocity vector is obtained by substituting Eq. (35) in Eq. (34) as

$$\mathbf{u}_f = \overline{\mathbf{u}_f} - \left(\nabla p_f - \overline{\nabla p_f}\right)\cdot\overline{\mathbf{D}_f} \tag{36}$$

The main feature of Eq. (36) is the dependence of the face velocity on the pressure of the adjacent cells, which avoids checkerboard patterns between velocity and pressure fields [20].

Substituting the face velocity, Eq. (36), obtained by Rhie-Chow interpolation, in Eq. (30), the continuity equation becomes

$$\sum_{f=nb(P)} \mathbf{S}_f\cdot\left\{\rho_f\left[\overline{\mathbf{u}_f} - \left(\nabla p_f - \overline{\nabla p_f}\right)\cdot\overline{\mathbf{D}_f}\right]\right\} = 0 \tag{37}$$

which can be expanded into

$$\begin{aligned}&\sum_{f=nb(P)} \mathbf{S}_f\cdot\left[\rho_f\left(-\nabla p_f\cdot\overline{\mathbf{D}_f}\right)\right] + \sum_{f=nb(P)} \mathbf{S}_f\cdot\left(\rho_f\overline{\mathbf{u}_f}\right)\\ &\quad= \sum_{f=nb(P)} \mathbf{S}_f\cdot\left[\rho_f\left(-\overline{\nabla p_f}\cdot\overline{\mathbf{D}_f}\right)\right]\end{aligned} \tag{38}$$

This leads to the algebraic equation with the following form:

$$\begin{aligned}&a_P^{pp}p_P + a_P^{pu}u_P + a_P^{pv}v_P + \sum_{F=NB(P)} a_F^{pp}p_F + \sum_{F=NB(P)} a_F^{pu}u_F\\ &\quad+ \sum_{F=NB(P)} a_F^{pv}v_F = b_P^p\end{aligned} \tag{39}$$

where $a_P^{p\phi}$ and $a_F^{p\phi}$ are respectively, the owner and neighbor coefficients in the discretized continuity equation representing the ϕ influence; and b_P^p is the source term, with the superscript p representing the pressure equation.

The pressure gradient part is discretized implicitly, similarly to what was done with the implicit diffusion term in the momentum equations (see page 86 of [56]). Hence,

$$\mathbf{S}_f\left[\cdot\rho_f\left(-\nabla p_f\cdot\overline{\mathbf{D}_f}\right)\right] = -\rho_f\frac{\mathbf{S}_f\cdot(\mathbf{S}_f\cdot\overline{\mathbf{D}_f})}{\mathbf{d}_{PF}\cdot\mathbf{S}_f}(p_F - p_P) \tag{40}$$

The coefficients of the implicit pressure gradient term for the continuity equation are given by

$$\begin{aligned}a_F^{pp} &= -\rho_f\frac{\mathbf{S}_f\cdot(\mathbf{S}_f\cdot\overline{\mathbf{D}_f})}{\mathbf{d}_{PF}\cdot\mathbf{S}_f}\\ a_P^{pp} &= -\sum_{F=NB(P)} a_{F,ipgrad}^{pp}\end{aligned} \tag{41}$$

The second term of Eq. (38) corresponding to the velocity contribution yields the following implicit coefficients

$$\begin{aligned}a_F^{pu} &= S_f^x\rho_f(1-g_f), \qquad a_F^{pv} = S_f^y\rho_f(1-g_f)\\ a_P^{pu} &= \sum_{f=nb(P)} S_f^x\rho_f g_f, \qquad a_P^{pv} = \sum_{f=nb(P)} S_f^y\rho_f g_f\end{aligned} \tag{42}$$

Finally, the coefficients of the explicit pressure gradient term contribution for the continuity equation are given by

$$b_P^p = \sum_{f=nb(P)} \mathbf{S}_f\cdot\left[\rho_f\left(-\overline{\nabla p_f}\cdot\overline{\mathbf{D}_f}\right)\right] \tag{43}$$

3.3. Discretization of the constitutive equation

The constitutive equation, Eq. (4), is first divided by the relaxation time, λ, yielding

$$\begin{aligned}&\left(\frac{1}{\lambda} + \frac{\epsilon}{\eta_P}\mathrm{tr}(\boldsymbol{\tau}_P)\right)\boldsymbol{\tau}_P + \frac{\partial\boldsymbol{\tau}_P}{\partial t} + \nabla\cdot(\mathbf{u}\boldsymbol{\tau}_P) = \frac{\eta_P}{\lambda}\left(\nabla\mathbf{u} + \nabla\mathbf{u}^T\right)\\ &\quad+\boldsymbol{\tau}_P\cdot\nabla\mathbf{u} + \nabla\mathbf{u}^T\cdot\boldsymbol{\tau}_P\end{aligned} \tag{44}$$

In the framework of the viscoelastic coupled solver here developed, the advective term in Eq. (44) is expanded in a way so that the velocity field would appear implicitly in the stress equation. For that, a second order Taylor series approximation for the functional $f(\mathbf{u},\boldsymbol{\tau}_P) = \mathbf{u}\boldsymbol{\tau}_P$ is used [57], to obtain

$$\nabla\cdot(\mathbf{u}\boldsymbol{\tau}_P) = \nabla\cdot(\boldsymbol{\tau}_P^0\mathbf{u}) + \nabla\cdot(\mathbf{u}^0\boldsymbol{\tau}_P) - \nabla\cdot(\mathbf{u}^0\boldsymbol{\tau}_P^0) \tag{45}$$

Hence, the constitutive equation, Eq. (44), is rewritten as

$$\begin{aligned}&\left(\frac{1}{\lambda} + \frac{\epsilon}{\eta_P}\mathrm{tr}(\boldsymbol{\tau}_P)\right)\boldsymbol{\tau}_P + \frac{\partial\boldsymbol{\tau}_P}{\partial t} + \nabla\cdot(\boldsymbol{\tau}_P^0\mathbf{u}) + \nabla\cdot(\mathbf{u}^0\boldsymbol{\tau}_P)\\ &\quad= \frac{\eta_P}{\lambda}\left(\nabla\mathbf{u} + \nabla\mathbf{u}^T\right) + \boldsymbol{\tau}_P\cdot\nabla\mathbf{u} +\\ &\quad+\nabla\mathbf{u}^T\cdot\boldsymbol{\tau}_P + \nabla\cdot(\mathbf{u}^0\boldsymbol{\tau}_P^0)\end{aligned} \tag{46}$$

which integrated over the control volume V gives

$$\begin{aligned}&\left(\frac{1}{\lambda} + \frac{\epsilon}{\eta_P}\mathrm{tr}(\boldsymbol{\tau}_P)\right)\int_V\boldsymbol{\tau}_P\,\mathrm{d}V + \int_V\frac{\partial\boldsymbol{\tau}_P}{\partial t}\,\mathrm{d}V + \int_V\nabla\cdot(\boldsymbol{\tau}_P^0\mathbf{u})\,\mathrm{d}V\\ &\quad+\int_V\nabla\cdot(\mathbf{u}^0\boldsymbol{\tau}_P)\,\mathrm{d}V\\ &\quad= \frac{\eta_P}{\lambda}\int_V\left(\nabla\mathbf{u} + \nabla\mathbf{u}^T\right)\mathrm{d}V + \int_V\left(\boldsymbol{\tau}_P\cdot\nabla\mathbf{u} + \nabla\mathbf{u}^T\cdot\boldsymbol{\tau}_P\right)\mathrm{d}V\\ &\quad+\int_V\nabla\cdot(\mathbf{u}^0\boldsymbol{\tau}_P^0)\,\mathrm{d}V\end{aligned} \tag{47}$$

Again, using the Gauss divergence theorem, the volume integrals of the flux divergences are transformed into surface integrals as

$$\left(\frac{1}{\lambda}+\frac{\epsilon}{\eta_P}\mathrm{tr}(\boldsymbol{\tau}_P)\right)\int_V \boldsymbol{\tau}_P\,\mathrm{d}V+\int_V\frac{\partial\boldsymbol{\tau}_P}{\partial t}\,\mathrm{d}V+\oint_S \mathbf{n}\cdot(\boldsymbol{\tau}_P^0\mathbf{u})\,\mathrm{d}S + \oint_S \mathbf{n}\cdot(\mathbf{u}^0\boldsymbol{\tau}_P)\,\mathrm{d}S = \frac{\eta_P}{\lambda}\int_V\left(\nabla\mathbf{u}+\nabla\mathbf{u}^T\right)\mathrm{d}V+\int_V\left(\boldsymbol{\tau}_P\cdot\nabla\mathbf{u}+\nabla\mathbf{u}^T\cdot\boldsymbol{\tau}_P\right)\mathrm{d}V + \oint_S \mathbf{n}\cdot(\mathbf{u}^0\boldsymbol{\tau}_P^0)\,\mathrm{d}S \tag{48}$$

Hence, the semi-discretized form of the extra-stress tensor constitutive equation is given by

$$V_P\left(\frac{1}{\lambda}+\frac{\epsilon}{\eta_P}\mathrm{tr}(\boldsymbol{\tau}_P^0)\right)\boldsymbol{\tau}_P+V_P\frac{\boldsymbol{\tau}_P-\boldsymbol{\tau}_P^0}{\Delta t}+\sum_{f=nb(P)}\mathbf{S}_f\cdot(\boldsymbol{\tau}_P^0\mathbf{u})_f + \sum_{f=nb(P)}\mathbf{S}_f\cdot(\mathbf{u}^0\boldsymbol{\tau}_P)_f = \frac{\eta_P V_P}{\lambda}\left(\nabla\mathbf{u}+\nabla\mathbf{u}^T\right)+V_P\left(\boldsymbol{\tau}_P\cdot\nabla\mathbf{u}+\nabla\mathbf{u}^T\cdot\boldsymbol{\tau}_P\right)+\sum_{f=nb(P)}\mathbf{S}_f\cdot(\mathbf{u}^0\boldsymbol{\tau}_P^0)_f \tag{49}$$

Finally, the equation is transformed into an algebraic equation by expressing the variable values and derivatives in terms of the owner (P) and neighbor (F) cells values. The discretized algebraic governing equation is given by

$$\begin{cases} a_P^{\tau_{xx}\tau_{xx}}(\tau_{xx})_P+a_P^{\tau_{xx}u}u_P+a_P^{\tau_{xx}v}v_P+\sum_{F=NB(P)}a_F^{\tau_{xx}\tau_{xx}}(\tau_{xx})_F+\sum_{F=NB(P)}a_F^{\tau_{xx}u}u_F + \sum_{F=NB(P)}a_F^{\tau_{xx}v}v_F=b_P^{\tau_{xx}} \\ a_P^{\tau_{xy}\tau_{xy}}(\tau_{xy})_P+a_P^{\tau_{xy}u}u_P+a_P^{\tau_{xy}v}v_P+\sum_{F=NB(P)}a_F^{\tau_{xy}\tau_{xy}}(\tau_{xy})_F+\sum_{F=NB(P)}a_F^{\tau_{xy}u}u_F + \sum_{F=NB(P)}a_F^{\tau_{xy}v}v_F=b_P^{\tau_{xy}} \\ a_P^{\tau_{yy}\tau_{yy}}(\tau_{yy})_P+a_P^{\tau_{yy}u}u_P+a_P^{\tau_{yy}v}v_P+\sum_{F=NB(P)}a_F^{\tau_{yy}\tau_{yy}}(\tau_{yy})_F+\sum_{F=NB(P)}a_F^{\tau_{yy}u}u_F + \sum_{F=NB(P)}a_F^{\tau_{yy}v}v_F=b_P^{\tau_{yy}} \end{cases} \tag{50}$$

where $a_P^{\epsilon\phi}$ and $a_F^{\epsilon\phi}$ are the owner and neighbor coefficients in the discretized polymeric extra-stress tensor equations representing the stress component ϵ and the variable ϕ interactions, respectively; and b_P^{ϵ} is the source term, with the superscript representing the ϵ polymeric extra-stress tensor component equation (for 2D cases $\epsilon=\{\tau_{xx},\tau_{xy},\tau_{yy}\}$, because the tensor $\boldsymbol{\tau}_P$ is symmetric, which means that $\tau_{xy}=\tau_{yx}$).

The first term (*stress*) in Eq. (49) contributes to the diagonal of the system of equations as

$$a_{P,stress}^{\tau_{xx}\tau_{xx}}=a_{P,stress}^{\tau_{xy}\tau_{xy}}=a_{P,stress}^{\tau_{yy}\tau_{yy}}=V_P\left(\frac{1}{\lambda}+\frac{\epsilon}{\eta_P}\mathrm{tr}(\boldsymbol{\tau}_P^0)\right) \tag{51}$$

The second term in Eq. (49), the rate of change (*rchg*), contributes to the diagonal of the system of equations as

$$a_{P,rchg}^{\tau_{xx}\tau_{xx}}=a_{P,rchg}^{\tau_{xy}\tau_{xy}}=a_{P,rchg}^{\tau_{yy}\tau_{yy}}=\frac{V_P}{\Delta t} \tag{52}$$

Additionally, the second term has an explicit contribution, which will be given below in Eq. (55).

The third term in Eq. (49) is discretized using a first-order Upwind scheme or a high-order CUBISTA scheme. Again, for the sake of readability, only the discretization with the Upwind scheme is shown. Hence, the coefficients of this implicit velocity term contribution for each component of the stress constitutive equations are given by

$$\begin{aligned} a_F^{\tau_{xx}u}&=\max(S_f^x(\tau_{xx}^0)_f,\,0), & a_F^{\tau_{xx}v}&=\max(S_f^y(\tau_{xx}^0)_f,\,0) \\ a_P^{\tau_{xx}u}&=-\sum_{F=NB(P)}a_F^{\tau_{xx}u}, & a_P^{\tau_{xx}v}&=-\sum_{F=NB(P)}a_F^{\tau_{xx}v} \\ a_F^{\tau_{xy}u}&=\max(S_f^x(\tau_{xy}^0)_f,\,0), & a_F^{\tau_{xy}v}&=\max(S_f^y(\tau_{xy}^0)_f,\,0) \\ a_P^{\tau_{xy}u}&=-\sum_{F=NB(P)}a_F^{\tau_{xy}u}, & a_P^{\tau_{xy}v}&=-\sum_{F=NB(P)}a_F^{\tau_{xy}v} \\ a_F^{\tau_{yy}u}&=\max(S_f^x(\tau_{yy}^0)_f,\,0), & a_F^{\tau_{yy}v}&=\max(S_f^y(\tau_{yy}^0)_f,\,0) \\ a_P^{\tau_{yy}u}&=-\sum_{F=NB(P)}a_F^{\tau_{yy}u}, & a_P^{\tau_{yy}v}&=-\sum_{F=NB(P)}a_F^{\tau_{yy}v} \end{aligned} \tag{53}$$

where we can define the volumetric flux $\dot{q}_{\boldsymbol{\tau}_P}=\mathbf{S}_f\cdot(\boldsymbol{\tau}_P^0)_f$, which will give the influence of each velocity component (u, v) in each component of the stress constitutive equations.

The fourth term in Eq. (49) is discretized also using the first-order upwind scheme or the CUBISTA scheme. Hence, the coefficients of the extra-stress tensor advection (*estadv*) term contribution for the stress constitutive equations are given by

$$\begin{aligned} a_{F,estadv}^{\tau_{xx}\tau_{xx}}&=a_{F,estadv}^{\tau_{xy}\tau_{xy}}=a_{F,estadv}^{\tau_{yy}\tau_{yy}}=\max(S_f^x u_f^0+S_f^y v_f^0,\,0) \\ a_{P,estadv}^{\tau_{xx}\tau_{xx}}&=-\sum_{F=NB(P)}a_{F,estadv}^{\tau_{xx}\tau_{xx}} \\ a_{P,estadv}^{\tau_{xy}\tau_{xy}}&=-\sum_{F=NB(P)}a_{F,estadv}^{\tau_{xy}\tau_{xy}} \\ a_{P,estadv}^{\tau_{yy}\tau_{yy}}&=-\sum_{F=NB(P)}a_{F,estadv}^{\tau_{yy}\tau_{yy}} \end{aligned} \tag{54}$$

where we can define the volumetric flux $\dot{q}_{\mathbf{u}}=\mathbf{S}_f\cdot\mathbf{u}_f^0$, which will give the influence of each stress component in the respective component of the stress constitutive equations.

All the terms on the right hand side of Eq. (49) are explicitly discretized, i.e., there is no implicit interaction from other stress components in the ϵ constitutive equation, except the ϵ component (see first terms of each equation in Eq. (50)). This fact does not limit the applicability of the numerical algorithm to other differential viscoelastic constitutive models (because these terms are explicitly discretized and not neglected), but in future studies the efficiency of the algorithm is expected to increase if the referred terms are implicitly discretized. Thus, the coefficients of the explicit extra-stress tensor terms contribution for the stress constitutive equations are given by

$$\begin{aligned} b_P^{\tau_{xx}}&=\frac{V_P\tau_{xx}^0}{\Delta t}+\frac{2\eta_P V_P}{\lambda}\frac{\partial u^0}{\partial x}+2V_P\left(\tau_{xx}^0\frac{\partial u^0}{\partial x}+\tau_{xy}^0\frac{\partial u^0}{\partial y}\right) + \sum_{f=nb(P)}\mathbf{S}_f\cdot(\mathbf{u}^0\tau_{xx}^0)_f \\ b_P^{\tau_{xy}}&=\frac{V_P\tau_{xy}^0}{\Delta t}+\frac{\eta_P V_P}{\lambda}\left(\frac{\partial v^0}{\partial x}+\frac{\partial u^0}{\partial y}\right) + V_P\left(\tau_{xx}^0\frac{\partial v^0}{\partial x}+\tau_{xy}^0\left(\frac{\partial v^0}{\partial y}+\frac{\partial u^0}{\partial x}\right)+\tau_{yy}^0\frac{\partial u^0}{\partial y}\right) + \sum_{f=nb(P)}\mathbf{S}_f\cdot(\mathbf{u}^0\tau_{xy}^0)_f \\ b_P^{\tau_{yy}}&=\frac{V_P\tau_{yy}^0}{\Delta t}+\frac{2\eta_P V_P}{\lambda}\frac{\partial v^0}{\partial y}+2V_P\left(\tau_{xy}^0\frac{\partial v^0}{\partial x}+\tau_{yy}^0\frac{\partial v^0}{\partial y}\right) + \sum_{f=nb(P)}\mathbf{S}_f\cdot(\mathbf{u}^0\tau_{yy}^0)_f \end{aligned} \tag{55}$$

Notice that the owner and neighbor coefficients related to extra-stress tensor component interactions are given by the sum of the stress, rate of change and advection terms contributions

$$a_\alpha^{\epsilon\phi}=a_{\alpha,stress}^{\epsilon\phi}+a_{\alpha,rchg}^{\epsilon\phi}+a_{\alpha,estadv}^{\epsilon\phi} \tag{56}$$

where ϵ and ϕ can be either τ_{xx}, τ_{xy} or τ_{yy} and α can be either P or F.

3.4. Coupled algorithm

Combining the discretized momentum (Eq. (10)), continuity (Eq. (39)) and stress constitutive (Eq. (50)) equations, the following system of equations, written in matrix form, is obtained for each control volume:

$$\begin{bmatrix} a_P^{uu} & a_P^{uv} & a_P^{up} & a_P^{u\tau_{xx}} & a_P^{u\tau_{xy}} & a_P^{u\tau_{yy}} \\ a_P^{vu} & a_P^{vv} & a_P^{vp} & a_P^{v\tau_{xx}} & a_P^{v\tau_{xy}} & a_P^{v\tau_{yy}} \\ a_P^{pu} & a_P^{pv} & a_P^{pp} & a_P^{p\tau_{xx}} & a_P^{p\tau_{xy}} & a_P^{p\tau_{yy}} \\ a_P^{\tau_{xx}u} & a_P^{\tau_{xx}v} & a_P^{\tau_{xx}p} & a_P^{\tau_{xx}\tau_{xx}} & a_P^{\tau_{xx}\tau_{xy}} & a_P^{\tau_{xx}\tau_{yy}} \\ a_P^{\tau_{xy}u} & a_P^{\tau_{xy}v} & a_P^{\tau_{xy}p} & a_P^{\tau_{xy}\tau_{xx}} & a_P^{\tau_{xy}\tau_{xy}} & a_P^{\tau_{xy}\tau_{yy}} \\ a_P^{\tau_{yy}u} & a_P^{\tau_{yy}v} & a_P^{\tau_{yy}p} & a_P^{\tau_{yy}\tau_{xx}} & a_P^{\tau_{yy}\tau_{xy}} & a_P^{\tau_{yy}\tau_{yy}} \end{bmatrix} \begin{bmatrix} u_P \\ v_P \\ p_P \\ (\tau_{xx})_P \\ (\tau_{xy})_P \\ (\tau_{yy})_P \end{bmatrix}$$
$$+ \sum_{F=nb(P)} \begin{bmatrix} a_F^{uu} & a_F^{uv} & a_F^{up} & a_F^{u\tau_{xx}} & a_F^{u\tau_{xy}} & a_F^{u\tau_{yy}} \\ a_F^{vu} & a_F^{vv} & a_F^{vp} & a_F^{v\tau_{xx}} & a_F^{v\tau_{xy}} & a_F^{v\tau_{yy}} \\ a_F^{pu} & a_F^{pv} & a_F^{pp} & a_F^{p\tau_{xx}} & a_F^{p\tau_{xy}} & a_F^{p\tau_{yy}} \\ a_F^{\tau_{xx}u} & a_F^{\tau_{xx}v} & a_F^{\tau_{xx}p} & a_F^{\tau_{xx}\tau_{xx}} & a_F^{\tau_{xx}\tau_{xy}} & a_F^{\tau_{xx}\tau_{yy}} \\ a_F^{\tau_{xy}u} & a_F^{\tau_{xy}v} & a_F^{\tau_{xy}p} & a_F^{\tau_{xy}\tau_{xx}} & a_F^{\tau_{xy}\tau_{xy}} & a_F^{\tau_{xy}\tau_{yy}} \\ a_F^{\tau_{yy}u} & a_F^{\tau_{yy}v} & a_F^{\tau_{yy}p} & a_F^{\tau_{yy}\tau_{xx}} & a_F^{\tau_{yy}\tau_{xy}} & a_F^{\tau_{yy}\tau_{yy}} \end{bmatrix} \begin{bmatrix} u_F \\ v_F \\ p_F \\ (\tau_{xx})_F \\ (\tau_{xy})_F \\ (\tau_{yy})_F \end{bmatrix} = \begin{bmatrix} b_P^u \\ b_P^v \\ b_P^p \\ b_P^{\tau_{xx}} \\ b_P^{\tau_{xy}} \\ b_P^{\tau_{yy}} \end{bmatrix} \tag{57}$$

The collection of all such systems over the entire computational domain results in a system of equations which size depends on the number of cells used, and can be written in the form $\mathbf{A\Phi} = \mathbf{b}$ where all variables $\mathbf{\Phi} = (\mathbf{u},\ p,\ \boldsymbol{\tau})$ are solved simultaneously. In this procedure all variables in the different equations are treated implicitly, which is expected to be advantageous for speed-up and stability of the overall calculation process. Moreover, the continuity equation is written in terms of pressure rather than pressure correction [58], because the system of equations computes all variables simultaneously. The algorithm used to solve the coupled governing equations can be summarized into the following steps:

1. Start with the latest available values ($\dot{m}_f^n,\ \dot{q}_{\boldsymbol{\tau}_p}^n,\ \dot{q}_{\mathbf{u}}^n,\ \mathbf{u}^n,\ p^n,\ \boldsymbol{\tau}^n$).
2. Assemble and solve the momentum, continuity and stress constitutive equations for $\mathbf{u}$, p and $\boldsymbol{\tau}$ (see Eqs. (10), (39), (50) and (57)).
3. Calculate $\dot{m}_f$, $\dot{q}_{\boldsymbol{\tau}_p}$ and $\dot{q}_{\mathbf{u}}$ using Eqs. (12), (53), (54).
4. Return to step 2 and repeat until convergence.

For the solution of the global system of discretized algebraic equations it is fundamental that an efficient linear solver is used in order to obtain the best overall convergence. In this work an algebraic multigrid solver (AMG) [59,60] with a block-ILU algorithm without fill-in [61], which works as a smoother in the multigrid cycle, are used, both for the coupled and segregated approaches.

4. Results and discussion

The performance of the viscoelastic coupled solver is assessed in three laminar, incompressible viscoelastic fluid flow problems: the planar Poiseuille flow of an Oldroyd-B fluid, the planar lid-driven flow of an Upper-Convected Maxwell (UCM) fluid and the 4:1 planar sudden contraction flow of a linear Phan-Thien-Tanner (LPTT) fluid. In addition, comparisons with the viscoelastic segregated solver based on the SIMPLE algorithm developed by Fernandes et al. [50] are presented. Notice that different SIMPLE-like algorithms, such as SIMPLER or SIMPLEC, could be used for a fairer comparison against the coupled solver, however only the original SIMPLE algorithm is currently implemented and validated on the foam-extend library [50,62]. The efficiency of the proposed coupled viscoelastic solver is demonstrated by comparing the number of iterations and CPU time required by each method on various computational grids, comprising different refinement levels. The same initial guess was used in all cases presented, and computations were stopped when the initial residual (RES) [63] of all variables ($\mathbf{\Phi}$) become smaller than 10^{-5}. RES is defined as

$$RES = \frac{\sum_{i=1}^{N} |\mathbf{b} - \mathbf{A\Phi}|}{n} \tag{58}$$

where N is the number of cells and n is the normalisation factor defined as

$$n = \sum_{i=1}^{N} \left(\left|\mathbf{A\Phi} - \mathbf{A}\overline{\mathbf{\Phi}}\right| + \left|\mathbf{b} - \mathbf{A}\overline{\mathbf{\Phi}}\right| \right) + \delta \tag{59}$$

where $\overline{\mathbf{\Phi}}$ is the arithmetic average of all the solution values $\mathbf{\Phi}$ in the domain and $\delta = 10^{-20}$ is a stabilization parameter to avoid divisions by zero. The initial residual for each iteration is evaluated based on the current values of the field, before solving the block-coupled system. After each block solver linear iteration, the residual is re-evaluated (final residual). When the maximum number of linear iterations (in this work defined as 100) or the final residual falls below the solver absolute tolerance (set as 10^{-9}), the block-coupled system current iteration stops and advances in time. The relaxation factors in the segregated runs were defined as 0.3 for pressure and stress and 0.7 for velocity, and in the coupled runs as 0.95 for velocity and stress and 1.0 for pressure, which in both cases correspond to the best performance in terms of computational time spent by the solvers.

The following discretization methods were used both in the segregated and coupled viscoelastic solvers. The time derivatives in the momentum and constitutive equations are discretized with the first-order implicit Euler scheme. The time marching is used only for relaxation purposes as the cases in this study are steady-state. As stated in Section 3 the advective terms in the momentum and constitutive equations are discretized using the first-order Upwind scheme or the high-order CUBISTA scheme. The diffusive term in the momentum equation is discretized using second-order accurate linear interpolation. A second-order Gaussian discretization is applied for source terms and for the gradients calculation. All computations were performed on a computer with a 3.40-GHz Intel Core i7-2600 CPU processor and 8 GB of RAM.

4.1. Poiseuille flow of an oldroyd-B fluid

The Poiseuille flow is an important benchmark case study for CFD code developers, because it often allows to obtain analytical solutions for fully developed flow conditions [64]. The geometry for this case is illustrated in Fig. 2 and consists of a channel with length L and half of the channel height H. In this work the ratio $L/H = 10$ was used. The

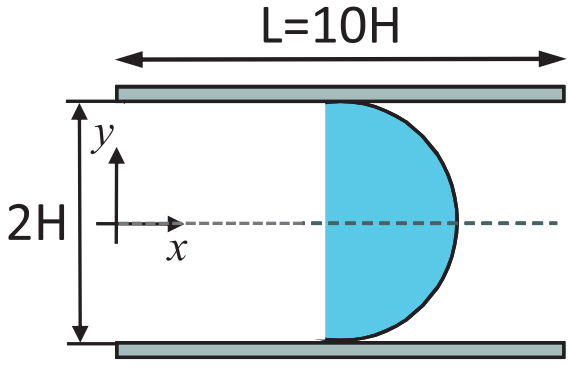

Fig. 2. Physical domain for the Poiseuille problem.

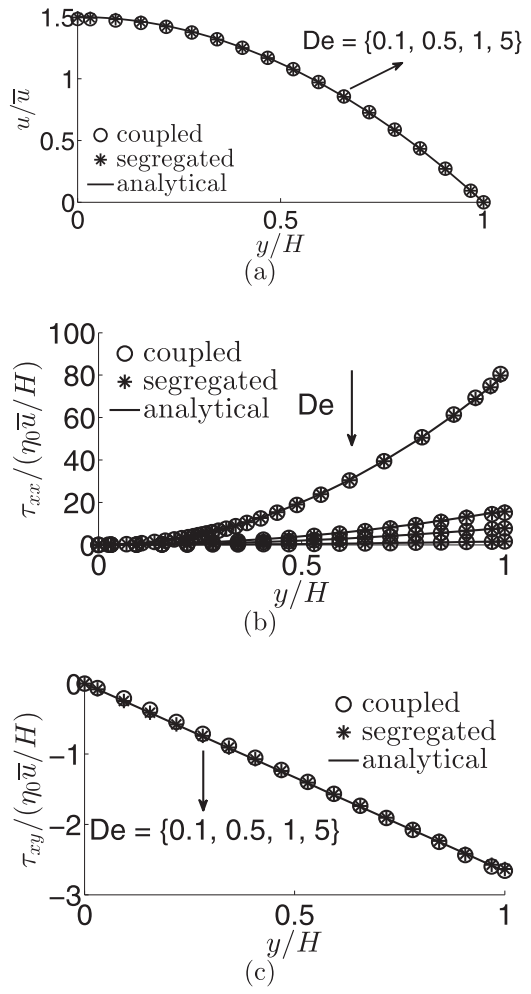

Fig. 3. Comparison of predicted (a) streamwise velocity and extra-stress tensor components (b) τ_{xx} and (c) τ_{xy}, using the segregated and coupled solvers, with analytical solutions for $De = \{0.1, 0.5, 1, 5\}$.

flow has a symmetry plane along the centerline ($y = 0$), to save computational resources and reduce the CPU time. The computations were done in three quadrilateral uniform grids with different levels of refinement, meshes M1, M2 and M3, with 2560 (160 × 16), 10240 (320 × 32) and 40960 (640 × 64) control volumes, respectively. The streamwise velocity component is u, the cross-stream velocity component is v, and the flow is defined in the (x, y)-plane with y representing the transversal coordinate. At the wall, $y = H$, the usual no-slip velocity is imposed and zero gradient is used both for pressure and extra-stress tensor fields (which does not affect the flow near the wall). At the inlet, a fully developed

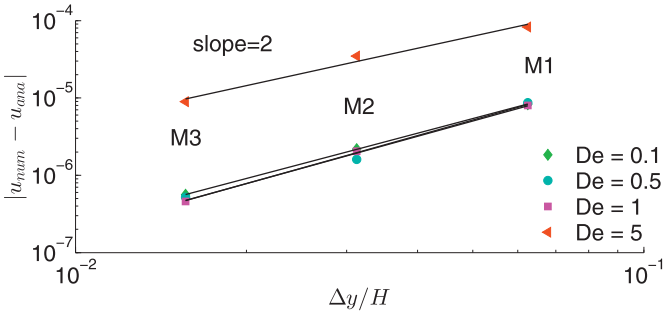

Fig. 4. Error as a function of the mesh resolution for the streamwise velocity component at $y = 0$. The solid lines represent linear fits to the values obtained in a log-log scale, thus its slope gives the convergence order.

velocity (see Eq. (60)), extra-stress tensor component (see Eqs. (62) and (63)) profiles and pressure gradient value (see Eq. (61)) are imposed. At the outlet, a uniform pressure with zero value is used and zero gradient is imposed both for velocity and extra-stress tensor fields. Finally, for all the computational cells, the initial values for all fields were set to zero. The problem is solved for a Reynolds number $Re \equiv \frac{\rho\overline{u}H}{\eta_0} = 0.01$, Deborah numbers of $De \equiv \frac{\lambda\overline{u}}{H} = \{0.1, 0.5, 1, 5\}$ and retardation ratio $\beta = \frac{1}{9}$, where $\overline{u}$ is the cross-sectional average velocity.

In fully developed flow, the velocities and stresses depend only on the transverse coordinate y (see [64]). The streamwise velocity profile is given by

$$u(y) = -\frac{p_x}{2\eta_P}\left(H^2 - y^2\right) \tag{60}$$

where p_x is the constant pressure gradient, which can be computed from

$$\overline{u} = \frac{-p_x H^2}{3\eta_P} \tag{61}$$

The two non-vanishing stress components are given by

$$\boldsymbol{\tau}_{xx} = \frac{2\lambda}{\eta_P} p_x^2 y^2 \tag{62}$$

$$\boldsymbol{\tau}_{xy} = p_x y \tag{63}$$

Results were validated by comparing the predictions generated by the coupled and segregated approaches at $x/L = 0.9$ against the analytical solutions, as shown in Fig. 3. As expected, the numerical streamwise velocity and the xy-component of the extra-stress tensor are invariant with the De number, contrarily to the extra-stress tensor xx-component. In addition, both methods (segregated and coupled) fall on top of each other and on the analytical solution, demonstrating the validity of the coupled solver.

In Fig. 4 we present the absolute value of the relative error of the streamwise velocity component u at $y = 0$, given by $|u_{num} - u_{ana}|$, as a function of the normalized cell size Δy. Notice that in fully developed flow conditions the advective terms vanish [65], and therefore the choice of the discretization scheme does not affect the convergence rate, even the Upwind scheme results in second-order convergence with respect to the grid size. Accordingly, the Poiseuille flow problem is not suitable to test the accuracy of the discretization schemes used for the advective terms, which will be assessed on the subsequent case study, the Lid-Driven Cavity.

A summary of the number of iterations and CPU time needed by the segregated and coupled approaches are presented for all De and grid sizes in Table 1. The ratio of the number of iterations required by the

Table 1
Comparison of the number of iterations and CPU time required by the segregated (S) and coupled (C) solvers for all De and grid sizes for the Oldroyd-B Poiseuille flow.

De	Mesh	Number of iterations			Execution time [s]		
		C	S	S/C	C	S	S/C
0.1	M1	106	764	7.2	16	33	2.0
	M2	454	5296	11.7	282	850	3.0
	M3	1373	34,873	25.4	4321	22,190	5.1
0.5	M1	291	2321	8.0	43	96	2.2
	M2	1112	13,629	12.3	654	2190	3.3
	M3	2820	83,902	29.8	7737	53,756	6.9
1	M1	489	6704	13.7	69	278	4.0
	M2	1868	30,645	16.4	990	4878	4.9
	M3	1431	153,336	107.2	4048	97,218	24.0
5	M1	3653	83,216	22.8	474	3370	7.1
	M2	451	78,431	173.9	279	12,570	45.1
	M3	1749	396,775	226.9	4805	252,160	52.5

M1: 2560 CV; M2: 10240 CV; M3: 40960 CV.

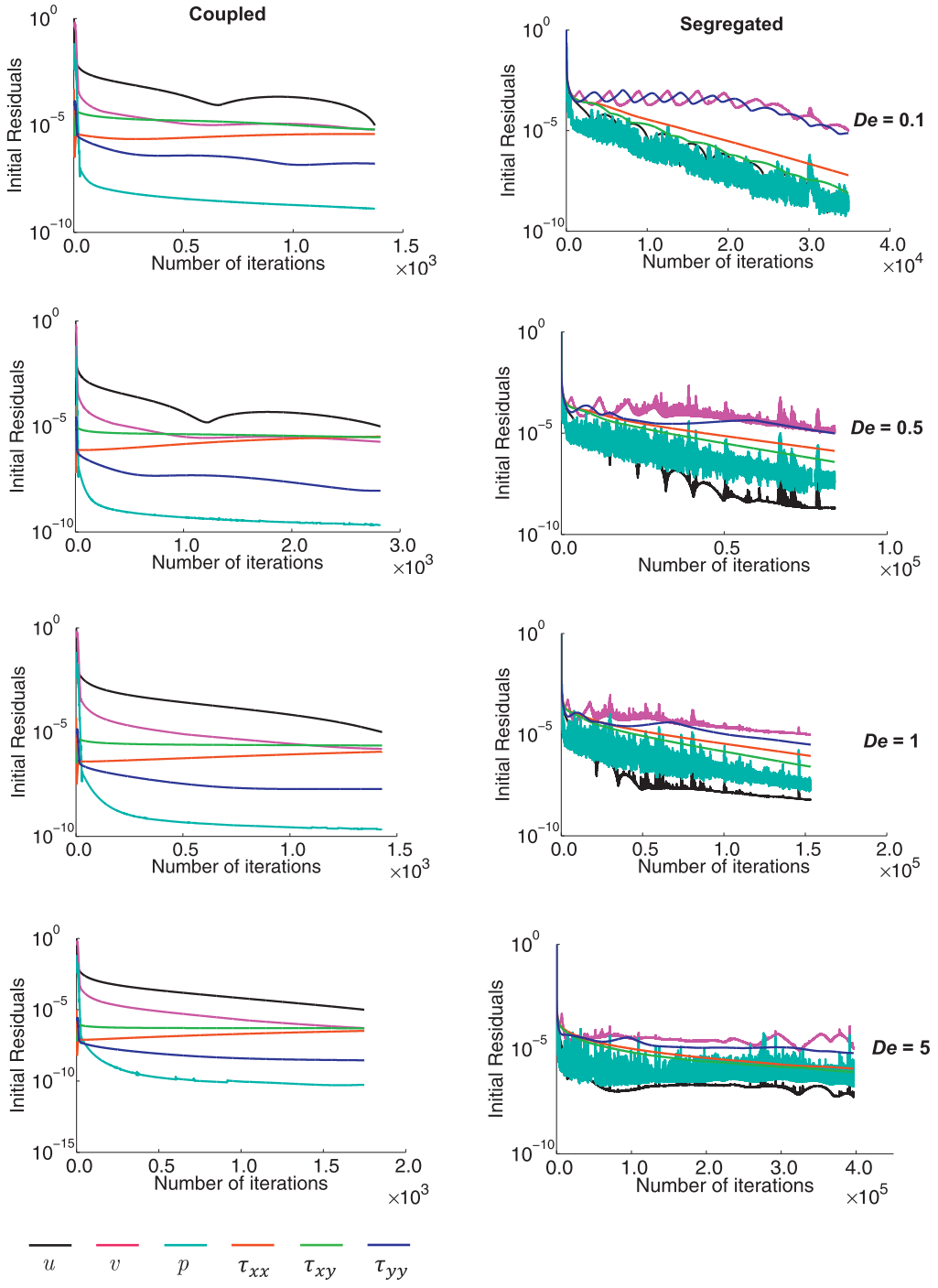

Fig. 5. Comparison of Oldroyd-B Poiseuille flow residual history plots with mesh M3 using coupled and segregated approaches for different $De = \{0.1, 0.5, 1, 5\}$.

segregated algorithm to that required by the coupled one (S/C) increases from 7.2 to 25.4, 8.0 to 29.8, 13.7 to 107.2, and 22.8 to 226.9 for $De = 0.1$, $De = 0.5$, $De = 1$ and $De = 5$, respectively. Hence, as the De number increases the gains of the coupled algorithm over the segregated one are higher, both in terms of number of iterations and CPU time. This is a direct consequence of the implicit coupling between velocity and extra-stress fields with the De. In addition, as the grid size increases from 2560 to 40,960 control volumes, the corresponding ratio of the CPU times needed increases from 2.0 to 5.1, 2.2 to 6.9, 4.0 to 24.0, and 7.1 to 52.5 for the tested De. This represents significant savings, as the total time required by the coupled approach to solve the four De number problems on the coarsest and densest grids used are 602 and 20,911 seconds, while those required by the segregated method are 3777 and 425,324 seconds, respectively, with the average S/C ratio varying from 6.3 to 20.3. This clearly shows the benefits obtained with the coupled approach.

The improved performance of the coupled solver is further demonstrated by the residual history plots of all the variables computed for all De in the densest grid, M3, presented in Fig. 5. As shown, the residual evolution with the coupled solver is smoother when compared to the segregated one, which results in an improved stable calculation, less prone to divergence. Moreover, we should stress that, in the graphs

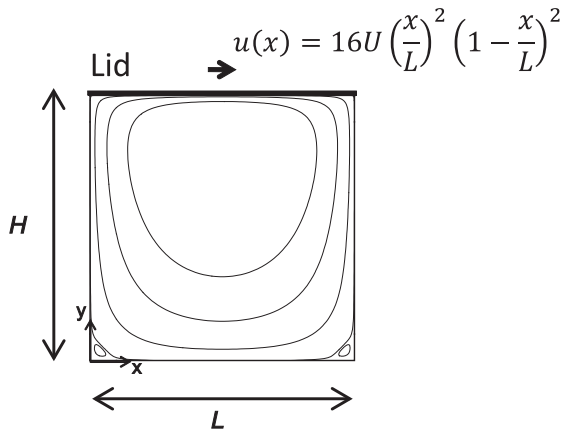

Fig. 6. Physical domain for the lid-driven cavity flow problem.

shown in Fig. 5, the *x*-axis are different by two orders of magnitude, when comparing coupled (left) and segregated (right) approaches, for the highest *De*.

4.2. Lid-driven cavity flow of an UCM fluid

The 2D fluid motion in a quadrangular channel induced by the translation of the lid (top wall) - the so-called lid-driven cavity flow - is a well-known benchmark problem for the validation of new numerical methods and techniques [66]. The geometry is shown schematically in Fig. 6 and comprises a two-dimensional rectangular channel of height H and width L, in which the top wall translates horizontally with a peak velocity U. In this work the aspect ratio H/L is set equal to one and four consistently refined quadrilateral uniform grids have been used, with the number of control volumes in grids M1, M2, M3 and M4 being equal to 1681 (41×41), 6889 (83×83), 27225 (165×165) and 108241 (329×329), respectively. Each mesh has an odd number of cells in both directions so that the variables are calculated exactly along the vertical and horizontal centrelines. The boundary conditions applied to the three stationary walls are no-slip and impermeability (i.e. $u = v = 0$, where u and v are the Cartesian components of the velocity vector). For the moving wall, a 4th order polynomial velocity regularization is used, such that both the velocity and the velocity gradient vanish at the corners [67]. The velocity regularization is given by

$$u(x) = 16U\left(\frac{x}{L}\right)^2\left(1-\frac{x}{L}\right)^2 \tag{64}$$

The pressure and extra-stress tensor fields were defined with zero gradient boundary condition at all the domain boundaries. The initial values for all fields were set to zero. The dimensionless groups defined for this case study are the $Re \equiv \rho UH/\eta_P$, because for the UCM model the solvent contribution is null ($\eta_S = 0$), and $De \equiv \lambda U/L$. The problem is solved for $Re = 0.01$ and $De = \{0.2, 0.4, 0.6\}$.

The resulting flow fields in the domain are visualized by the streamline maps presented in Fig. 7. As shown, the two sets of contours fall almost on top of each other confirming the validity of the developed coupled approach. In addition, the implementation was validated by comparing the predictions generated by the coupled and segregated solvers for the velocity distribution along the channel lines $x/L = 0.5$ and $y/H = 0.5$, and for the polymeric extra-stress tensor components along $y/H = 0.99$. As shown in Figs. 8 and 9, the results provided by both solvers (segregated and coupled) overlap, demonstrating the correct implementation of the coupled solver.

In Fig. 10 we present the absolute value of the error for the minimum streamwise velocity component u at $x/L = 0.5$, given by $|u_{\min} - u^{ext}_{\min}|$, and for the maximum transversal velocity component v at $y/H = 0.5$, given by $|v_{\max} - v^{ext}_{\max}|$, as a function of the normalized cell size $\Delta x/L$, where *ext* denotes the extrapolated value using Richardson extrapolation [68] (see Table 2). The calculations were performed using the Upwind and CUBISTA schemes, for the discretization of the advection term, being the order of convergence computed for both schemes. Additionally, the results of Sousa et al. [67] using a segregated approach and the CUBISTA scheme are plotted for comparison purposes. As can be seen in Fig. 10 the results obtained using the developed coupled algorithm are in line with the theoretical order of convergence of the UDS and CUBISTA schemes, which is 1 and 3 (on uniform grids) or 2 (on non-uniform grids), respectively.

A summary of the number of iterations and CPU time needed by the segregated and coupled approaches are presented for all *De* and grid sizes in Table 3. The ratio of the number of iterations required by the segregated algorithm to that required by the coupled one (S/C) is nearly constant in each *De*, except for M4 with $De = 0.6$, which shows a value of 14.4. As for the Poiseuille flow case study (Section 4.1) the tendency of the S/C ratio is to increase with *De*, which seems to be a clear advantage of the viscoelastic coupled algorithm. In addition, as the grid size increases from 1681 to 108,241 control volumes, the corresponding ratio of the CPU time needed by the segregated solver to that required by the coupled one tends to increase, from 1.3 to 1.5, 1.3 to 2.0, and 1.4 to 5.5 for the *De* tested. Again, a huge saving as the total time required by the coupled approach to solve the three *De* number problems on the coarsest and densest grids used are 2428 and 459,418 seconds, while those required by the segregated method are 3204 and 1,576,202 seconds, with the average S/C ratio varying from 1.3 to 3.4. Again, the benefits of the coupled over the segregated approach are visible, both in terms of number of iterations and CPU time, and also by the residual history plots of all the variables computed for all *De* numbers with the densest grid, M4, presented in Fig. 11. The above findings are in line with the results reported in [20,21,23], for the performance of the pressure-velocity coupled solver on structured and unstructured grids, and a clear indication of a successful extension to viscoelastic flows.

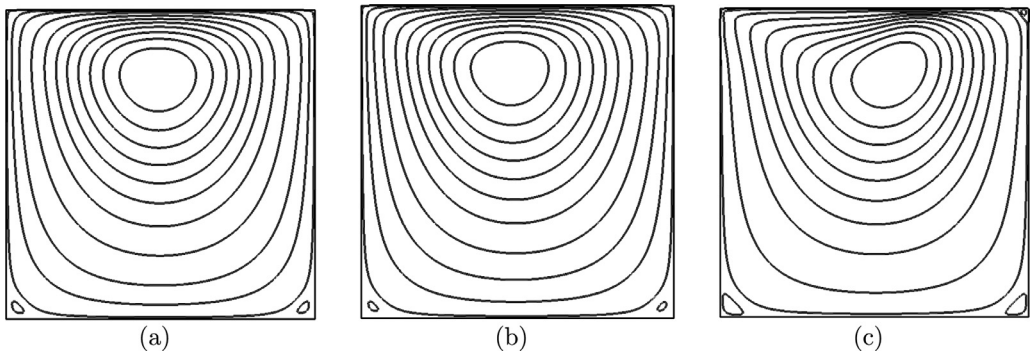

Fig. 7. Computed streamlines for the UCM lid-driven cavity flow using coupled (grey line) and segregated (black line) approaches, with mesh M4, for (a) $De = 0.2$, (b) $De = 0.4$ and (c) $De = 0.6$.

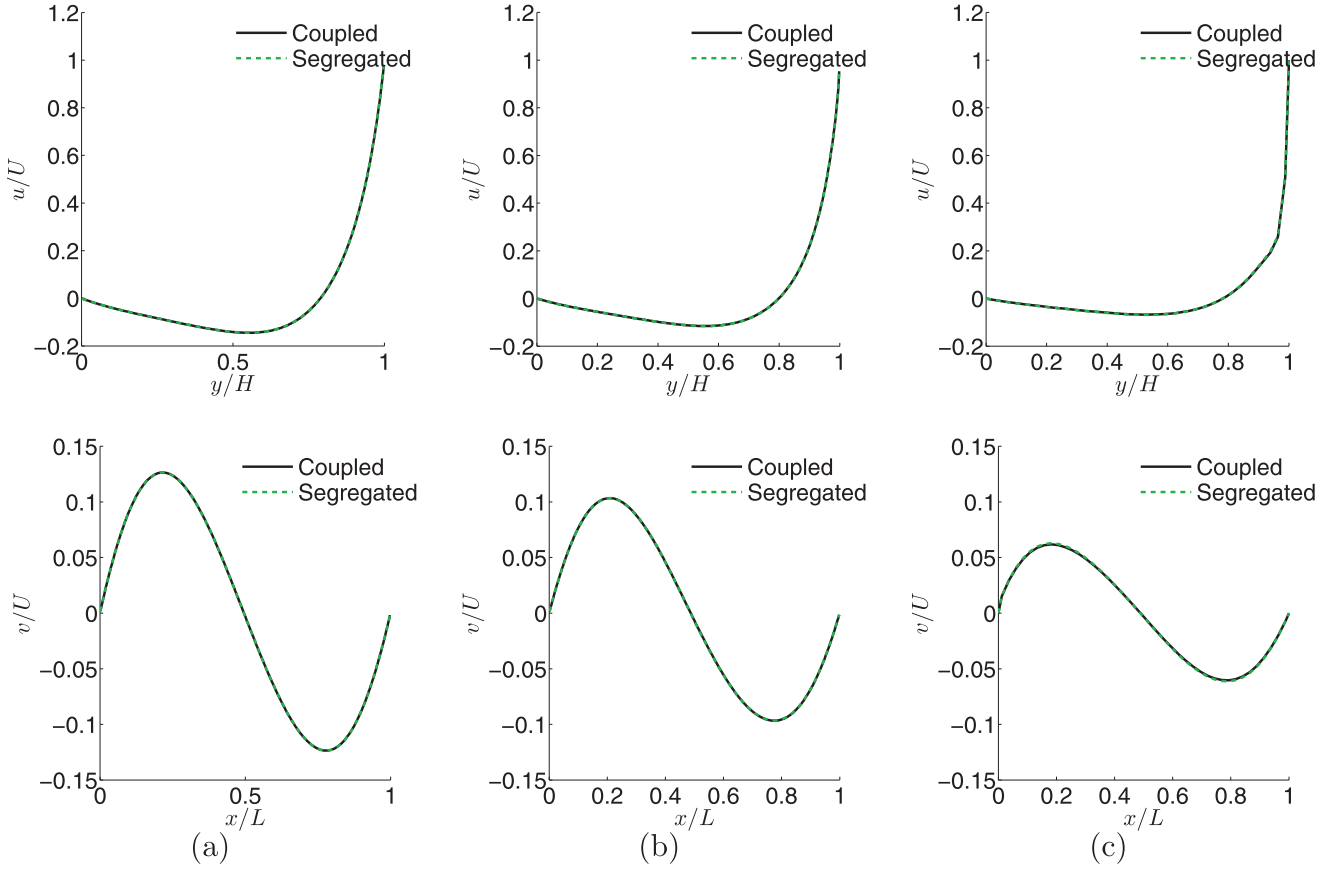

Fig. 8. Comparison of predicted velocity components at $x/L = 0.5$ (top) and $y/H = 0.5$ (bottom) using segregated and coupled approaches, with mesh M4, for (a) $De = 0.2$, (b) $De = 0.4$ and (c) $De = 0.6$.

Table 2
Effect of mesh refinement on: minimum values of u computed along $x/L = 0.5$ and maximum values of v computed along $y/H = 0.5$ for $De = 0.4$, using Upwind and CUBISTA discretization schemes.

Mesh	Coupled algorithm			Segregated algorithm [67]		
	Upwind		CUBISTA		CUBISTA	
	u_{min}/U	v_{max}/U	u_{min}/U	v_{max}/U	u_{min}/U	v_{max}/U
M1	−0.112007	0.100735	−0.111177	0.0996204	−0.116698	0.104745
M2	−0.1128	0.100807	−0.1115	0.0996436	−0.117251	0.105013
M3	−0.1145	0.102062	−0.114396	0.101896	−0.117398	0.105118
M4	−0.115853	0.103426	−0.115806	0.103387	−0.117412	0.105109
Extrapolated	−0.117206	0.10479	−0.116276	0.103884	−0.117417	0.105106

Table 3
Comparison of the number of iterations and CPU time required by the segregated and coupled flow solvers for all De and grid sizes for the UCM lid-driven cavity flow.

De	Mesh	Number of iterations			Execution time [s]		
		C	S	S/C	C	S	S/C
0.2	M1	6830	31,012	4.5	555	694	1.3
	M2	7523	38,196	5.1	3523	6100	1.7
	M3	9554	40,653	4.3	21,031	34,684	1.7
	M4	10,248	43,402	4.2	103,625	151,045	1.5
0.4	M1	11,374	58,811	5.2	863	1112	1.3
	M2	12,632	70,410	5.6	5383	10,462	1.9
	M3	14,955	81,276	5.4	30,395	65,633	2.2
	M4	16,481	84,709	5.1	149,065	295,347	2.0
0.6	M1	15,197	85,000	5.6	1010	1398	1.4
	M2	17,167	116,282	6.8	6697	12,497	1.9
	M3	21,112	139,422	6.6	38,234	84,394	2.2
	M4	25,145	362,526	14.4	206,728	1,129,810	5.5

M1: 1681 CV; M2: 6889 CV; M3: 27225 CV; M4: 108241 CV.

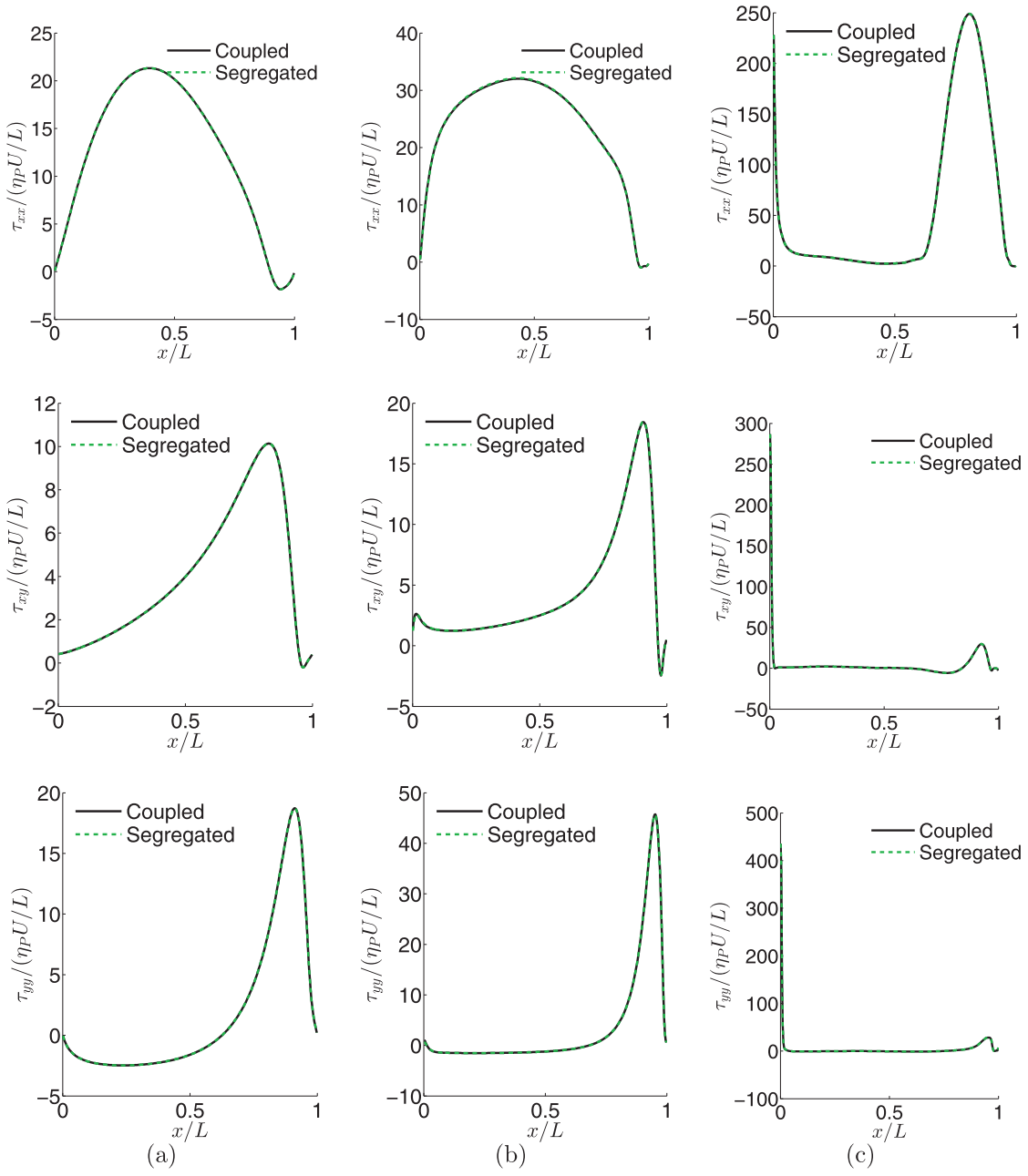

Fig. 9. Comparison of predicted polymeric extra-stress tensor components at $y/H = 0.99$ using segregated and coupled approaches, with mesh M4, for (a) $De = 0.2$, (b) $De = 0.4$ and (c) $De = 0.6$.

4.3. LPTT Fluid flow in a 4:1 planar sudden contraction geometry

The 2D fluid motion in a sudden contraction geometry with contraction ratio $CR = H_1/H_2 = 4$ is the last case study to be performed in this work, and it is appropriate to expose shear-extension interaction [69] and possible numerical instability of the developed code. A sketch of the contraction geometry is illustrated in Fig. 12, where only half of the two-dimensional domain is used for the computations, with symmetry conditions imposed at the centreline, $y = 0$. The half-width of the shorter channel H_2 is taken as the characteristic length scale, and the average velocity in that channel, U_2, is the characteristic velocity scale. For this case study, the CUBISTA scheme is used for the discretization of the velocity and extra-stress tensor advective terms.

The computations have been performed on two meshes, with higher refinement near the walls and in the contraction region, because these two regions are known to present the highest gradients of the flow variables. The meshes employed are similar to the ones used on a previous study [50], being the total number of control volumes equal to 942 and 3598, which correspond to a minimum mesh spacing of $\Delta x_{\min} = \Delta y_{\min} = 0.04H_2$ and $0.02H_2$, respectively.

The viscoelastic coupled solver is tested for increasing values of the Deborah number $De \equiv \lambda U_2/H_2 = \{1, 5, 10, 20, 50, 100\}$ but for a constant Reynolds number $Re \equiv \rho U_2 H_2/\eta_0 = 0.01$, representative of creeping flow conditions. The linear PTT model with viscosity ratio $\beta = 1/9$ and extensional parameter $\epsilon = 0.25$, typical of polymer melts, is used.

The following boundary conditions were used for all the runs performed: for velocity, no-slip at the walls, symmetry at the centerline, fully-developed profile at the inlet (with average velocity $U_1 = U_2/CR$) (see Eq. (60)), and a zero gradient condition at the outlet, i.e., assuming fully-developed flow; for pressure, fixed pressure gradient at the inlet

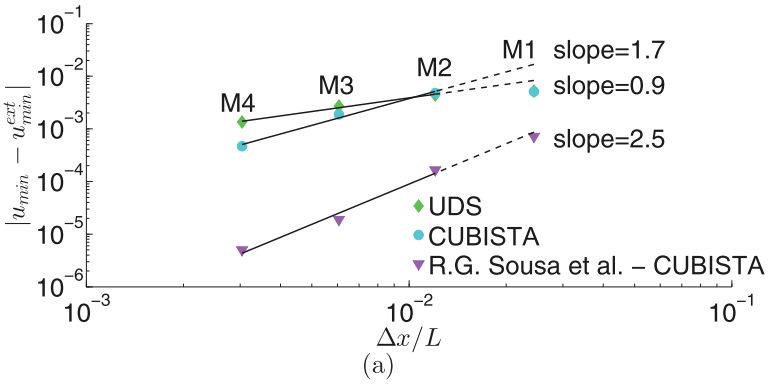

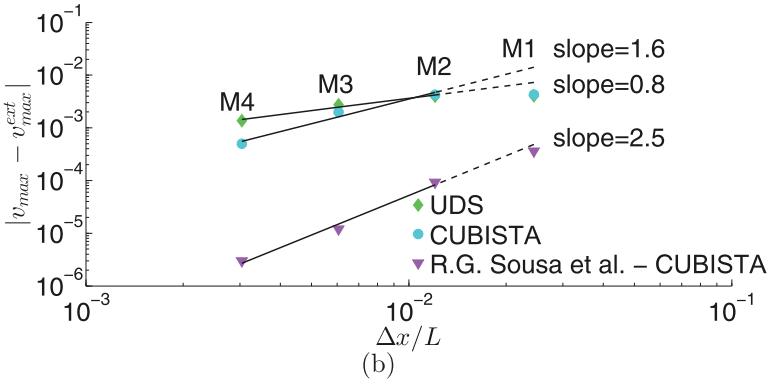

Fig. 10. Error as a function of the mesh resolution for the (a) minimum value of the streamwise velocity component u at $x/L = 0.5$ and for the (b) maximum value of the transversal velocity component v at $y/H = 0.5$ for $De = 0.4$. The solid lines represent linear fits to the values obtained with meshes M2-M4 in a log-log scale, thus its slope gives the convergence order. The dashed lines are an extrapolation of the linear fit.

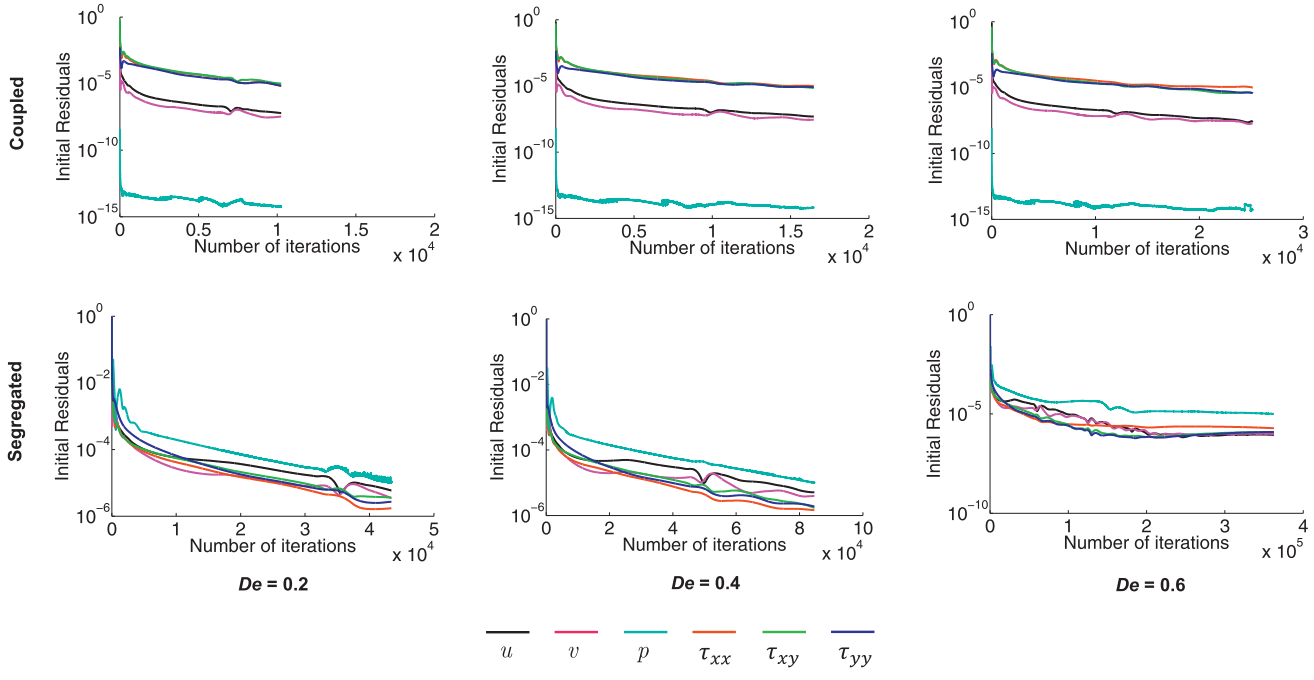

Fig. 11. Comparison of UCM lid-driven cavity residual history plots with mesh M4 using coupled and segregated approaches for different $De = \{0.2, 0.4, 0.6\}$.

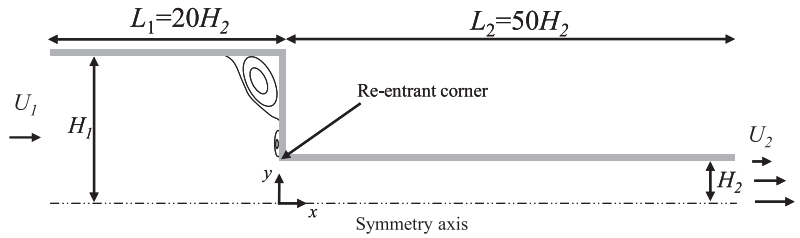

Fig. 12. Schematic representation of the 4:1 planar sudden contraction.

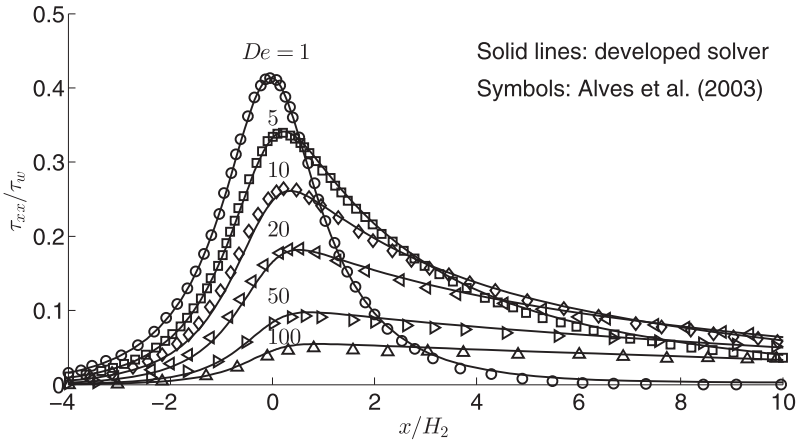

Fig. 13. Distribution of the axial normal stress τ_{xx} for the linear PTT model with $\epsilon = 0.25$ along the centreline.

(see Eq. (61)), zero gradient at the wall, symmetry boundary condition at the centerline and fixed value, $p = 0$, at the outlet; finally, for the stress tensor, fully-developed profiles at the inlet (see Eqs. (62) and (63)), symmetry boundary condition at the centerline, and zero gradient condition at the walls and outlet. All internal fields were set to zero at the initial time.

Fig. 13 presents the longitudinal profiles along the centreline ($y = 0$) of the axial normal stress component (τ_{xx}), normalised with $\tau_w \equiv 3\eta_0 U_2/H_2$, for all the *De* numbers tested. For comparison purposes, the data of Alves et al. [70] is also plotted in the figure, which shows a fair agreement with minor differences in the downstream channel, thus further validating the newly developed viscoelastic coupled solver.

A summary of the number of iterations and CPU time required by the segregated and coupled approaches are presented for all *De* and grid sizes in Table 4. The results obtained show again the benefits of the coupled over the segregated approach, both in terms of number of iterations and CPU time. Moreover, Fig. 14 show the residual history plots of all the variables computed for $De = \{1, 50, 100\}$ with the densest grid M2.

Table 4
Comparison of the number of iterations and CPU time required by the segregated and coupled flow solvers for all *De* and grid sizes for the LPTT fluid flow in a 4:1 planar sudden contraction geometry.

De	Mesh	Number of iterations			Execution time [s]		
		C	S	S/C	C	S	S/C
1	M1	14,908	92,398	6.2	845	1238	1.5
	M2	14,846	120,445	8.1	5024	6183	1.2
5	M1	23,847	176,584	7.4	1047	2373	2.3
	M2	23,621	303,233	12.8	6472	15,675	2.4
10	M1	28,585	175,940	6.2	1064	2359	2.2
	M2	28,275	217,102	7.7	6336	11,912	1.9
20	M1	33,823	109,547	3.2	1040	1596	1.5
	M2	33,441	182,394	5.5	6475	9990	1.5
50	M1	41,298	104,388	2.5	1028	1536	1.5
	M2	40,812	156,659	3.8	7079	9795	1.4
100	M1	47,133	67,289	1.4	906	969	1.1
	M2	46,517	169,526	3.6	7285	10,456	1.4

M1: 942 CV; M2: 3598 CV.

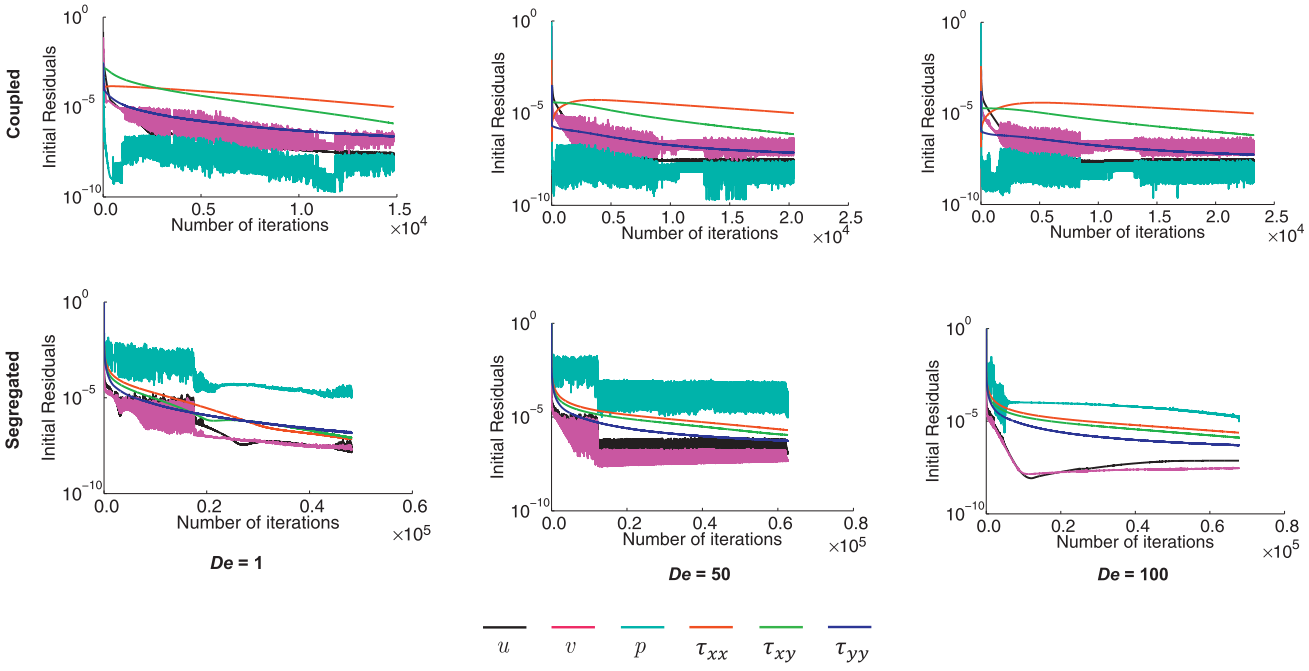

Fig. 14. Comparison of LPTT 4:1 planar sudden contraction residual history plots with mesh M2 using coupled and segregated approaches for different $De = \{1, 50, 100\}$.

Again, the limiting variable in the convergence of the segregated solver is the pressure field, which is related to the iterative approach used to solve the governing equations.

5. Conclusions

This paper presented a fully coupled method for the solution of laminar incompressible viscoelastic flows on collocated grids. The method was newly developed and implemented in the open-source computational library foam-extend, a community driven fork of the OpenFOAM software. The coupled solver is a pressure-based method in which the pressure equation is derived in the same way as in the SIMPLE algorithm, the explicit diffusion term added by the iBSD technique to the momentum equation is discretized with a special second order derivative of the velocity field, and the convective term in the extra-stress tensor constitutive equation is approximated with a second order Taylor series expansion.

The performance of the coupled algorithm was demonstrated with three laminar incompressible viscoelastic fluid flow problems: Oldroyd-B Poiseuille, UCM lid-driven cavity and LPTT 4:1 sudden contraction planar flows. The performance of coupled and segregated solvers was compared in terms of number of iterations and CPU time required to obtain a solution converged to a predefined level. The results showed that the computational time and number of iterations required by the coupled solver are significantly lower than those needed by the segregated one. This represents huge savings as the ratio of the calculation time (segregated/coupled) range from 2.0 to 52.5 for the Oldroyd-B Poiseuille flow, from 1.3 to 5.5 for the UCM lid-driven cavity flow, and from 1.1 to 2.4 for the LPTT 4:1 sudden contraction flow. In addition, the benefits were found to increase with the grid refinement and Deborah number, a feature that further evidences the pertinence of the proposed approach. This is particularly important when dealing with practical scenarios (e.g. industrial-sized problems). Lastly, the results obtained from the coupled and segregated approaches have been shown to be nearly equal, and a fair comparison is also obtained with other results found in the scientific literature, which allowed to validate the present implementation.

In future works the extension of the algorithm to circumvent the high Weissenberg number problem and to improve the implicitness of the extra-stress constitutive equation will be addressed, and 3D case studies with unstructured meshes are also envisaged.

Acknowledgments

This work is funded by UID/CTM/50025/2013 - LA0025, with the financial support of FCT/MEC through national funds and when applicable by FEDER co-funded, within the partnership agreement PT2020. The authors would like to acknowledge the Minho University cluster under the project Search-ON2: Revitalization of HPC infrastructure of UMinho, (NORTE-07-0162-FEDER-000086), co-funded by the North Portugal Regional Operational Programme (ON.2-0 Novo Norte), under the National Strategic Reference Framework (NSRF), through the European Regional Development Fund (ERDF).

Appendix

To show the independence of the results on the artificial diffusivity, $\eta^\star$, added by the improved both-sides diffusion (iBSD) methodology, we employed the Poiseuille flow case study (presented in Section 4.1), with a quantitative comparison of the stress and pressure drop for different values of $\eta^\star$. This way, the stress component at the wall (τ_{xx} at $y = H$) and the pressure drop, for three different values of the artificial diffusivity, $\eta^\star = \{\eta_P, 10\eta_P, 100\eta_P\}$ were computed. The relative error between the numerical results and the analytical solution (see Eqs. (61) and (62)) is presented in Tables 5 and 6, respectively, for the τ_{xx} and pressure drop, and for the different tested values of $\eta^\star$, De and mesh densities.

Table 5
Comparison between numerical τ_{xx} stress component (Pa) at $y = H$ and analytical solution for $\eta^\star = \{\eta_P, 10\eta_P, 100\eta_P\}$. The values between parentheses are the relative errors (%) computed as $error = 100 \times (\tau_{xx}^{analytic} - \tau_{xx}^{numeric})/\tau_{xx}^{analytic}$.

$\eta^\star$	De	M1	M2	M3
η_P	0.1	0.000636369 (0.6)	0.000640142 (0.02)	0.000639915 (0.01)
	0.5	0.00318168 (0.6)	0.00319969 (0.01)	0.0031991 (0.03)
	1	0.00636158 (0.6)	0.00640067 (0.01)	0.00639553 (0.07)
$10\eta_P$	0.1	0.000634404 (0.9)	0.000640824 (0.1)	0.000641218 (0.2)
	0.5	0.00317179 (0.9)	0.00320349 (0.1)	0.00318213 (0.6)
	1	0.00634206 (0.9)	0.00640678 (0.1)	0.00640301 (0.05)
$100\eta_P$	0.1	0.000619046 (3.3)	0.000636936 (0.5)	0.000640991 (0.2)
	0.5	0.00309412 (3.3)	0.00318433 (0.5)	0.0032011 (0.03)
	1	0.0061878 (3.3)	0.00636829 (0.5)	0.00640898 (0.1)

M1: 2560 CV; M2: 10240 CV; M3: 40960 CV.

Table 6
Comparison between numerical pressure drop (Pa) and analytical solution for $\eta^\star = \{\eta_P, 10\eta_P, 100\eta_P\}$. The values between parentheses are the relative errors (%) computed as $error = 100 \times (\Delta P^{analytic} - \Delta P^{numeric})/\Delta P^{analytic}$.

$\eta^\star$	De	M1	M2	M3
η_P	0.1	0.0123116 (2.6)	0.0121778 (1.5)	0.0120936 (0.8)
	0.5	0.0121965 (1.6)	0.0121108 (0.9)	0.0120572 (0.5)
	1	0.0116638 (2.8)	0.0117555 (2.0)	0.0118117 (1.6)
$10\eta_P$	0.1	0.0123388 (2.8)	0.0122073 (1.7)	0.0121137 (0.9)
	0.5	0.0122463 (2.1)	0.0121479 (1.2)	0.0120709 (0.6)
	1	0.0116703 (2.7)	0.011766 (1.9)	0.01184 (1.3)
$100\eta_P$	0.1	0.0122334 (1.9)	0.0121924 (1.6)	0.012122 (1.0)
	0.5	0.0121938 (1.6)	0.0121572 (1.3)	0.0120907 (0.8)
	1	0.0119209 (0.7)	0.01195 (0.4)	0.0119566 (0.4)

M1: 2560 CV; M2: 10240 CV; M3: 40960 CV.

These results show that the relative errors are less than 3.3% for all the cases tested and, in general, decrease with mesh refinement, which confirms, as desired, the independence of the results on the artificial diffusivity.

References

[1] R.B Bird, R.C Armstrong, O. Hassager, Dynamics of Polymeric Liquids, 1, 2 edition, John Wiley & Sons, New York, 1987.
[2] P. Wesseling, Principles of Computational Fluid Dynamics, Springer Series in Computational Mathematics, 29, Springer-Verlag Berlin Heidelberg, 2001.
[3] A.J Chorin, Numerical Solution of the Navier-Stokes Equations, Math. Comput. 22 (1968) 745–762.
[4] R. Temam, Sur l'approximation de la solution des équations de navier-stokes par la méthode des pas fractionnaires II, Arch. Ration. Mech. Anal. 33 (1969) 377–385.
[5] S.V Patankar, D.B Spalding, A calculation procedure for heat, mass and momentum transfer in three-dimensional parabolic flows, Int. Heat Mass Transf. 15 (1972) 1787–1806.
[6] S.V Patankar, Numerical Heat Transfer and Fluid Flow, Hemisphere, New York, 1981.
[7] C. Hsu, A Curvilinear-Coordinate Method for Momentum, Heat and Mass Transfer in Domains of Irregular Geometry, University of Minnesota, Minneapolis, MN, 1981 Ph.D. thesis.

[8] C. Rhie, W. Chow, Numerical study of turbulent flow past an isolated airfol with trailing edge separation, AIAA J. 21 (1983) 1525–1532.
[9] J.P.V. Doormaal, G.D. Raithby, Enhancement of the SIMPLE method for prediciting incompressible fluid flows, Numer. Heat Transfer Part B 7 (1984) 147–163.
[10] R.I Issa, Solution of the implicitly discretised fluid flow equations by operator-splitting, J. Comput. Phys. 62 (1986) 40–65.
[11] J. van Kan, A second-order accurate pressure-correction scheme for viscous incompressible flow, SIAM J. Sci. Stat. Comput. 7 (1986) 870–891.
[12] W. Rodi, S. Majumdar, B. Schonung, Finite volume methods for two-dimensional incompressible flows with complex boundaries, Comput. Meth. Appl. Mech. Eng. 75 (1989) 369–392.
[13] E.J Dean, R. Glowinski, On some finite element methods for the numerical simulation of incompressible viscous flow, in: M. Gunzburger, R. Nicolaides (Eds.), Incompressible Computational Fluid Dynamics: Trends and Advances, Cambridge University Press, 1993.
[14] F. Moukalled, M. Darwish, A unified formulation of the segregated class of algorithms for fluid flow at all speeds, Numer. Heat Transfer Part B 37 (2000) 103–139.
[15] J.P.V. Doormaal, Numerical Methods for the Solution of Incompressible and Compressible Fluid Flows, University of Waterloo, 1985 Ph.D. thesis.
[16] R.D Lonsdale, An algebraic multigrid scheme for solving the navier-stokes equations on unstructured meshes, Proc. 7th Int. Conf. on Numerical Methods in Turbulent and Laminar Flows (1991) 1432–1442.
[17] R. Webster, An algebraic multigrid solver for navier-stokes problems, Int. J. Numer. Meth. Fluids 18 (1994) 761–780.
[18] R. Webster, An algebraic multigrid solver for navier-stokes problems in the discrete second-order approximation, Int. J. Numer. Meth. Fluids 22 (1996) 1103–1123.
[19] I. Ammara, C. Masson, Development of a fully coupled control-volume finite element method for the incompressible navier-stokes equations, Int. J. Numer. Meth. Fluids 44 (2004) 621–644.
[20] M. Darwish, I. Sraj, F. Moukalled, A coupled incompressible flow solver on structured grid, Numer. Heat Transfer Part B 52 (2007) 353–371.
[21] M. Darwish, I. Sraj, F. Moukalled, A coupled finite volume solver for the solution of incompressible flows on unstructured grids, J. Comput. Phys. 228 (2009) 180–201.
[22] Z.J Chen, A.J Przekwas, A coupled pressure-based computational method for incompressible/compressible flows, J. Comput. Phys. 229 (2010) 9150–9165.
[23] L. Mangani, M. Buchmayr, M. Darwish, Development of a novel fully coupled solver in openFOAM: steady-state incompressible turbulent flows, Numer. Heat Transfer Part B 66 (2014) 1–20.
[24] D.L Brown, R. Cortez, M.L Minion, Accurate projection methods for the incompressible navier-stokes equations, J. Comp. Phys. 168 (2001) 464–499.
[25] H.H Hu, D.D Joseph, Numerical simulation of viscoelastic flow past a cylinder, J. Non-Newtonian Fluid Mech. 37 (1990) 347–377.
[26] X. Huang, N. Phan-Thien, R.I Tanner, Viscoelastic flow between eccentric rotating cylinders: unstructured control volume method, J. Non-Newtonian Fluid Mech. 64 (1996) 71–92.
[27] K.A Missirlis, D. Assimacopoulos, E. Mitsoulis, A finite volume approach in the simulation of viscoelastic expansion flows, J. Non-Newtonian Fluid Mech. 78 (1998) 91–118.
[28] P.J Oliveira, F.T Pinho, G.A Pinto, Numerical simulation of non-linear elastic flows with a general collocated finite-volume method, J. Non-Newtonian Fluid Mech. 79 (1998) 1–43.
[29] P.J Oliveira, F.T Pinho, Plane contraction flows of upper convected maxwell and phan-thien-tanner fluids as predicted by a finite-volume method, J. Non-Newtonian Fluid Mech. 88 (1999) 63–88.
[30] M.A Alves, F.T Pinho, P. Oliveira, Effect of a high-resolution differencing scheme on finite-volume predictions of viscoelastic flows, J. Non-Newtonian Fluid Mech. 93 (2000) 287–314.
[31] M.A Alves, F.T Pinho, P.J Oliveira, The flow of viscoelastic fluids past a cylinder: finite-volume high-resolution methods, J. Non-Newtonian Fluid Mech. 97 (2001) 207–232.
[32] F. Dupret, J.M Marchal, M.J Crochet, On the consequence of discretization errors in the numerical calculation of viscoelastic flow, J. Non-Newtonian Fluid Mech. 18 (1985) 173–186.
[33] F. Dupret, J.M Marchal, Loss of evolution in the flow of viscoelastic fluids, J. Non-Newtonian Fluid Mech. 20 (1986) 143–171.
[34] J. van der Zanden, M. Hulsen, Mathematical and physical requirements for successful computations with viscoelastic fluid models, J. Non-Newtonian Fluid Mech. 29 (1988) 93–117.
[35] M.A Hulsen, A sufficient condition for a positive definite configuration tensor in differential models, J. Non-Newtonian Fluid Mech. 38 (1990) 93–100.
[36] R. Keunings, Advances in the computer modeling of the flow of polymeric liquids, Comp. Fluid Dyn. J. 9 (2001) 449–458.
[37] K. Walters, M.F Webster, The distinctive CFD challenges of computational rheology, Int. J. Numer. Meth. Fluids 43 (2003) 577–596.
[38] E.O.A Carew, P. Townsend, M.F. Webster, A Taylor-Petrov-galerkin algorithm for viscoelastic flow, J. Non-Newtonian Fluid Mech. 50 (1993) 253–287.
[39] P. Wapperom, M.F. Webster, A second-order hybrid finite-element/volume method for viscoelastic flows, J. Non-Newtonian Fluid Mech. 79 (1998) 405–431.
[40] P. Wapperom, M.F Webster, Simulation for viscoelastic flow by a finite volume/element method, Comp. Meth. Appl. Mech. Eng. 180 (1999) 281–304.
[41] M. Aboubacar, H. Matallah, M.F Webster, Highly elastic solutions for oldroyd-b and phan-thien/tanner fluids with a finite volume/element method: planar contraction flows, J. Non-Newtonian Fluid Mech. 103 (2002) 65–103.
[42] M. Aboubacar, H. Matallah, H.R Tamaddon-Jahromi, M.F Webster, Numerical prediction of extensional flows in contraction geometries: hybrid finite volume/element method, J. Non-Newtonian Fluid Mech. 104 (2002) 125–164.
[43] A. Afonso, P.J Oliveira, F.T Pinho, M.A Alves, The log-conformation tensor approach in the finite-volume method framework, J. Non-Newtonian Fluid Mech. 157 (2009) 55–65.
[44] R.F Hanby, D.J Silvester, A comparison of coupled and segregated iterative solution techniques for incompressible swirling flow, Int. J. Numer. Methods Fluids 22 (1996) 353–373.
[45] L.S Caretto, R.M Curr, D.B Spalding, Two numerical methods for three-dimensional boundary layers, Comput. Methods Appl. Mech. Engrg. 1 (1972) 39–57.
[46] M.E Braaten, Development and Evaluation of Iterative and Direct Methods for the Solution of the Equations Governing Recirculating Flows, University of Minnesota, 1985 Ph.D. thesis.
[47] S.P Vanka, Block-implicit multigrid solution of navier-stokes equations in primitive variables, J. Comput. Phys. 65 (1986) 138–158.
[48] K.C Karki, H.C Mongia, Evaluation of a coupled solution approach for fluid flow calculations in boddy fitted coordinates, Int. J. Numer. Methods Fluids. 11 (1990) 1–20.
[49] Z. Mazhar, A procedure for the treatment of the velocity-pressure coupling problem in incompressible fluid flow, Numer. Heat Transf., Part B 39 (2001) 91–100.
[50] C. Fernandes, M.S.B. Araujo, L.L. Ferrás, J.M. Nóbrega, Improved both sides diffusion (iBSD): a new and straightforward stabilization approach for viscoelastic fluid flows, J. Non-Newtonian Fluid Mech. 249 (2017) 63–78.
[51] foam-extend, Open source CFD toolbox, 2013 https://sourceforge.net/projects/foam-extend/.
[52] N. Phan-Thien, R.I Tanner, A new constitutive equation derived from network theory, J. Non-Newtonian Fluid Mech. 2 (1977) 353–365.
[53] J.G. Oldroyd, On the formulation of rheological equations of state, Proc. R. Soc. London A 200 (1950) 523–541.
[54] R. Guénette, M. Fortin, A new mixed finite element method for computing viscoelastic flows, J. Non-Newtonian Fluid Mech. 60 (1995) 27–52.
[55] M.A Alves, P.J Oliveira, F.T Pinho, A convergent and universally bounded interpolation scheme for the treatment of advection, Int. J. Numer. Meth. Fluids 41 (2003) 47–75.
[56] H. Jasak, Error Analysis and Estimation for the Finite Volume Method with Applications to Fluid Flows, Imperial College University of London, 1996 Ph.D. thesis.
[57] P. Seeburger, Calcplot3d, an exploration environment for multivariable calculus - taylor polynomials of a function of two variables (1st and 2nd degree), Convergence (2011).
[58] K. Jareteg, V. Vukčević, H. Jasak, pUCoupledFoam - an open source coupled incompressible pressure-velocity solver based on foam-extend, 9th OpenFOAM Workshop, Zagreb, Croatia, 2014.
[59] A. Jemcov, J.P. Maruszewski, H. Jasak, Stabilization of agglomerative algebraic multigrid solver by recursive projection method, 13th Copper Mountain Conference on Multigrid Methods, 2007.
[60] Y. Notay, An aggregation–based algebraic multigrid method, Electron. Trans. Numer. Anal. 37 (2010) 123–146.
[61] Y. Saad, Iterative Methods for Sparse Linear Systems (2nd edition), Society for Industrial and Applied Mathematics Philadelphia, SIAM, 2003.
[62] J.L Favero, A.R Secchi, N.S.M Cardozo, H. Jasak, Viscoelastic flow analysis using the software openFOAM and differential constitutive equations, J. Non-Newton. Fluid Mech. 165 (2010) 1625–1636.
[63] openfoam, The open source CFD toolbox, http://www.openfoam.com/documentation/cpp-guide/html/guide-solvers-residuals.html 2017.
[64] P.J Oliveira, F.T Pinho, Analytical solution for fully developed channel and pipe flow of phan-thien-tanner fluids, J. Fluid Mech. 387 (1999) 271–280.
[65] F. Habla, M.W Tan, J. Haßlberger, O. Hinrichsen, Numerical simulation of the viscoelastic flow in a three-dimensional lid-driven cavity using the log-conformation reformulation in openFOAM, J. Non-Newton. Fluid Mech. 212 (2014) 47–62.
[66] P.N Shankar, M.D. Deshpande, Fluid mechanics in the driven cavity, Ann. Rev. Fluid Mech. 32 (2000) 93–136.
[67] R.G Sousa, R.J Poole, A.M Afonso, F.T Pinho, P.J Oliveira, A. Morozov, M. Alves, Lid-driven cavity flow of viscoelastic liquids, J. Non-Newtonian Fluid Mech. 234 (2016) 129–138.
[68] JH. Ferziger, M. Peric, Computational Methods for Fluid Dynamics, 3 edition, Springer-Verlag, Berlin Heidelberg, 2002.
[69] R.I. Tanner, Engineering Rheology, Oxford Engineering Science Series, 2 edition, Oxford University Press, 2000.
[70] M.A Alves, P.J Oliveira, F.T Pinho, Benchmark solutions for the flow of oldroyd-b and PTT fluids in planar contractions, J. Non-Newtonian Fluid Mech. 110 (2003) 45–75.